2016

Inlet Distortion Effects on the Unsteady Aerodynamics of a Transonic Fan Stage

Daniel Oliver Reilly
Wright State University

INLET DISTORTION EFFECTS ON THE UNSTEADY AERODYNAMICS OF A TRANSONIC FAN STAGE

A thesis submitted in partial fulfillment of the
requirements for the degree of Master of Science in
Mechanical Engineering

By

DANIEL OLIVER REILLY
B.S.M.E., Wright State University, 2015

2016
Wright State University

WRIGHT STATE UNIVERSITY

GRADUATE SCHOOL

August 29, 2016

I HEREBY RECOMMEND THAT THE THESIS PREPARED UNDER MY SUPERVISION BY Daniel Oliver Reilly ENTITLED Inlet Distortion Effects on the Unsteady Aerodynamics of a Transonic Fan Stage BE ACCEPTED IN PARTIAL FULFILLMENT OF THE REQUIREMENTS FOR THE DEGREE OF Master of Science in Mechanical Engineering

_____

Mitch Wolff, Ph.D.
Thesis Director

_____

Joseph Slater, Ph.D.
Chair, Department of Mechanical
and Materials Engineering

Committee on
Final Examination

_____

David A. Johnston, Ph.D.

_____

George Huang, Ph.D.

_____

Robert E. W. Fyffe, Ph.D.
Vice President for Research and
Dean of the Graduate School

ABSTRACT

Reilly, Daniel Oliver. M.S.M.E. Department of Mechanical and Materials Engineering, Wright State University, 2016. Inlet Distortion Effects on the Unsteady Aerodynamics of a Transonic Fan Stage.

A computational study was conducted to understand the influence of aircraft inlet distortion flow on the unsteady aerodynamic loading of a gas turbine fan stage. A single stage, transonic fan design with no inlet guide vanes was modeled with a commercial, computational fluid dynamics solver, STAR-CCM+, using the harmonic balance technique. The baseline inlet boundary condition applied to the model is consistent with that of a homeomorphic variant of the M2129 S-duct, and exhibited stagnation pressure distortion and a swirl pattern. The baseline inlet flow was decomposed and parameterized into a set of inlet boundary conditions which were individually applied in a series of computational runs. The parametric effect of the swirl velocity on the unsteady aerodynamic loading of the fan blade was studied. The flow structure at 90% span was investigated and revealed localized flow patterns in the blade row. A Fourier analysis revealed that the inlet distortion did not simply convect with the flow, but changed strength along the streamline, redistributing the spectral energy of the pressure and velocity components, and was dependent on the swirl parameter value. The inlet distortion also caused the passage shock to move up to 12% of the blade chord. Finally, the first six harmonics of the inlet distortion contributed significantly to the aerodynamic loading of the transonic fan.

TABLE OF CONTENTS

LIST OF FIGURES

LIST OF TABLES

ACKNOWLEDGEMENTS

I thank my advisors, Dr. David Johnston and Dr. Mitch Wolff, for all the support and time they have dedicated to this project. I truly appreciate the tremendous amount of learning opportunities I received because of them.

I thank my family and friends for always believing in my abilities and urging me to do my best.

I thank King James for coming home and bringing the title to Cleveland.

NOMENCLATURE

AIP	=	aerodynamic interface plane
a	=	swirl distortion parameter
CFD	=	computational fluid dynamics
HB	=	harmonic balance
N	=	nodal diameter
M	=	number of regional harmonics
$(w_1, m_1 m_2)$	=	user-defined regional harmonics
(N_W, N_R, N_S)	=	fundamental engine order of each region (1, 20, 31)
N	=	truncated Fourier series harmonic
P	=	pressure
Q	=	velocity magnitude
ROM	=	reduced order method
(r,θ,z)	=	polar coordinate system
t	=	time
(U, V, W)	=	axial, tangential, radial velocity components
w_n	=	Fourier coefficients of the solution
w_k^*	=	time periodic solution
ω	=	excitation frequency
(x,y,z)	=	Cartesian coordinate system components
D/B	=	axial distance / axial chord

1. INTRODUCTION

1.1 Motivation

Embedded aircraft engines of next generation aircraft have the potential to significantly reduce fuel burn and mask unwanted noise pollution. But, complications arise with embedded engines due to the intensification of fluid distortion associated with the fuselage, nacelle, and intake duct. Airframe body and engine inlet ducts are known to distort the flow and affect engine performance and operability. Inlet distortion and engine compatibility is a design requirement for aircraft engine system integration. Furthermore, as shown in various studies [Besem 2015, Danforth 1974, Hamed 1997], upstream airframe geometry and ducted inlets cause blade vibration in the first few stages of a gas turbine engine, with the potential to exceed safe excitation levels.

Inlet distortions caused by aircraft maneuvers have proven to cause blade row resonant vibrations near a natural frequency and in turn cause fatigue failure of blades. [Smith 2015] Inlet distortion influences on the engine aeromechanical response and stability is therefore a durability concern [SAE 2013, Hamed 1997, Danforth 1974, Manwaring 1997]. Under dynamic stresses resulting from an upstream distortion, fatigue failure is a major concern to the fan when vibrating at its natural frequency or high oscillation engine order [SAE 2010].

As seen in Figure 1, the commercial transport jet features podded engines while the D8 experimental aircraft features embedded engines. Podded engine fans ideally receive uniform free-stream flow. Embedded engines on the other hand tend to receive varying regions of velocity and pressure distortion stemming from upstream airframe geometries disturbing the uniform (or “clean”) inlet flow.

Figure 1 - a: Commercial transport showing podded engines. b: D8 NASA concept exhibiting embedded engines. (Photo credit- a: woodward.com b: Nasa.gov)

The aeroelastic interaction and unsteady stress can be predicted using computational fluid dynamic (CFD) and finite element analysis (FEA) solvers. This thesis focuses on the unsteady aerodynamics using CFD. Predicting the unsteady aerodynamic forces that cause blade vibration is a key component in the advancement of modeling blade aeromechanics [Smith 2015].

Modeling the aerodynamic effects via transient simulations of a full annulus with multiple blade rows can be done, but is computationally expensive when using time-marching methods. Several engine rotations of time-marching require many computational iterations and a large computation time for an accurate solution. In contrast to the time-marching solution method, to a reduced order, frequency domain, harmonic balance (HB) method reduces the computation time requirement while producing results that are within engineering accuracy [Hall 2002]. Consequently, the HB method will be used in this study.

1.2 Objective

The goal of this research is to gain insight into the influence of the swirl component of aircraft inlet flow distortion on the aerodynamic and vibrational loading of a fan stage. In particular, the unsteady aerodynamics generated in a transonic fan stage will be investigated to better understand how inlet distortions affect fan aeromechanics.

1.3 Approach

The computational domain of a single sector blade was used in a CFD model to simulate the flow field under the influence of an inlet distortion boundary condition using the harmonic balance solver technique. A baseline inlet flow distortion was selected which is consistent with one produced by a homeomorphic variant of the M2129 S-duct. The pattern exhibited stagnation pressure distortion and twin swirl. This baseline inlet flow distortion was parameterized by using a method that constrains the flow kinetic energy at the boundary to remain constant, while varying the swirl strength, directly proportional to the parameter setting.

Four parametric settings of the swirl where specified and applied as inlet boundary conditions to the model in a series of computational runs. Flow variables were recorded and used to dissect the effects of the inlet distortion on blade loading patterns, flow structure, and modal forces. The results of these simulations were interrogated to study the unsteady blade loading and flow fields as a function of the swirl intensity at the inlet.

1.4 Organization

Chapter 1 provides an introduction to this study. Chapter 2 provides key concepts in understanding inlet distortions, a literature review, and the governing flow physics formulation. Chapter 3 provides a description of the geometry and meshing techniques. Chapter 4 provides a modal and mesh sensitivity study as well as the distortion forcing functions. Chapter 5 presents the distortion parametric solutions with an emphasis on the transonic fan aeromechanics. Chapter 6 summarizes the thesis concluding with a discussion of the key findings.

2. BACKGROUND

2.1 Literature Review

2.1.1 Inlet Distortion Flow

Experimental boundary layer ingestion work was began as early as 1947 in an article by Smith and Roberts and has the potential to reduce fuel burn of an engine by 5% in N+2 and 10% in N+3 aircraft [Smith 2015, Bakhle 2014]. The embedded engine setup can provide system level benefits by re-energizing the momentum wake behind the aircraft. Aircraft that employ ducted inlets as well as aircraft concepts with integrated engines, such as the D8 concept [Uranga 2014], experience distorted inlet condition regions with unusual velocity swirl components due to upstream airframe components [Ferrar 2011].

These embedded-engine aircraft were researched due to their single-plane momentum change benefits. Aircraft that use podded engines affect the surrounding air on two different planes causing a low momentum wake region to the stern of the fuselage and a high momentum propulsor region to the stern of the engine [Arntz 2014]. This results in large amounts of wasted kinetic energy. Embedding the engines is a solution to this kinetic energy loss as it combines the wake and propulsor to the same momentum plane and mitigates wasted kinetic energy [Arntz 2014].

Furthermore, much of the published work to date was centered on N+2 generation aircraft that exhibit a blended wing body with an embedded engine. Research accomplished by Hardin et al on ultra-high bypass propulsion systems under the influence of an inlet distortion showed that on compact-inlet, aft-mounted propulsion systems using a bypass ratio between 15 and 18, and a

pressure ratio of between 1.25 and 1.35, a fuel burn reduction of up to 10% was possible for N+3 generation aircraft [Hardin 2012].

Distortion patterns arise with the usage of S-duct geometry upstream of the fan stage. Numerical solutions to the M2129 diffusing S-duct were investigated by Mohler in an effort to test the Wind-US flow solver [Mohler 2004]. An unstructured grid was used in a time accurate steady state model [Mohler 2004]. Predicted flow fields showed separation along the lower surface of the duct causing a vortex distortion pattern at the exit boundary. Furthermore, it was shown that predicted pressure recovery and inlet distortion were consistent with experimental results.

Further, experimental research on an S-duct was completed by Ferrar and tested various mass flow rates. Results were similar to CFD simulations where curvature in the duct affects the static pressure gradient due to flow separation [Ferrar 2011]. It was shown that separation at the AIP can be significant and concluded that knowing the velocity and pressure gradients are required to predict blade loadings [Ferrar 2011].

In CFD research by Peterson, a full annulus URANS simulation of a fan (rotor 4) with varying inlet distortions was compared to a single passage HB solution [Peterson 2016]. The results of the study confirmed the near equivalence of URANS and HB simulations. Looking further into this study, it was found that using more harmonic modes in the wake distortion specification undoubtedly modeled the flow physics more accurately. Peterson characterizes the research as a "stepping stone for further optimization of the HB method".

Accurately predicting inlet flow distortion is a key to predicting blade resonance response [Sanders 2013]. From steady and unsteady RANS CFD simulations Sanders predicted flow development of an S-duct and compared the predictions to experimental data. It was shown that

vortices shed off the side walls lead to swirl patterns at the start of the fan. Comparing experimental and numerical results, an 8% difference was noted, leaving the numerical solution well within engineering accuracy. The one per-rev distortion was shown to be reliably predicted using STAR-CCM+ HB [Sanders 2013].

2.1.2 Blade Aeromechanics

While the system level benefits were obvious, the inlet distortion tolerance of the engine turbomachinery is important in making the reduction in fuel burn occur. System level benefits could be diminished due to deficits in the compression system performance. Bakhle found that engineering quantities such as inlet total pressure loss, fan efficiency reduction, and fan stall margin reduction all govern the fan ability to aide in fuel burn reduction [Bakhle 2012]. Furthermore, aeromechanic responses of the compressor must be within acceptable limits in distorted flow caused by the upstream impedance for embedded engines to have any significant benefits [Hardin 2012].

In a study completed by Bakhle et al, a structural model was analyzed using an inlet distortion boundary under ducted flow conditions. Reynolds-averaged Navier Stokes (RANS) computational fluid dynamic software was used to model fan aerothermodynamic and aeromechanical aspects of intermediate design iterations operating with a boundary layer ingesting inlet [Bakhle 2012]. The decoupled analysis method yielded predictions for the model baseline fan flutter and forced response characteristics [Bakhle 2012].

A complementary study by Bakhle et al investigated blade fatigue failure due to alternating stress [Bakhle 2014]. A RANS analysis was used to investigate a distortion tolerant fan, which could be suitable for wind tunnel testing [Bakhle 2014]. A forced response analysis explored the static and dynamic stresses due to an inlet distortion and concluded that engine

order excitations were strong in the unsteady simulation for a seventh engine order excitation, however, excitation energy reduced quickly after the third harmonic.

2.1.3 Techniques for Fast CFD

CFD research aimed at providing an alternative to the computationally expensive of time-marching methods led to the formulation of a HB technique. Hall et al. developed this technique in the early 2000's and the technique has recently been implemented in commercial CFD codes [Hall 2007].

The HB technique allows the analyst to model unsteady, nonlinear flows in periodic repeating patterns using Fourier transforms of unsteady flow conservation variables [Hall 2007]. Using a time-linearized technique, the time derivatives of the Navier-Stokes equations are linearized about an average flow solution and the time derivatives are replaced with the frequency of unsteadiness so as to remove the physical time stepping requirement [Hall 2007]. This process is highlighted in Section 2.3. While the method sacrificed nonlinear accuracy in the Fourier component decomposition, it allowed for the analyst to control the number of harmonics used in the simulation, resulting in tailoring the solution accuracy for the intended model [Hall 2007]. The method has been shown to accurately predict the effects of both unsteady blade vibration and the forced response produced when influenced by upstream wake interaction [Custer 2009].

Studies using the STAR-CCM+ implicit coupled, nonlinear HB method have proven to reliably predict unsteady flow structures at less computational cost compared to the full annulus, unsteady simulation [Custer 2012, Weiss 2011]. HB and proper orthogonal decomposition (POD) techniques are forms CFD aiming at reducing computation time and speeding up the computational design process [Lucia 2004, Burkardt 2003]. Both methods aim to reduce

computation time but do so in different ways for in HB the time domain is reduced through Fourier transforms while in POD, the spatial domain is reduced. For this reason HB is a "fast method" while POD is a Reduced order method (ROM). The accurate prediction of flutter and forced response drives the need for these fast/ROM unsteady flow solvers in the domain of aeromechanics [He 2010].

Computer models with millions of degrees of freedom are implemented on supercomputers due to the modern advancement in computing power [Lucia 2004]. Flow structure in three dimensions for physical problems is consistently simulated numerically for simpler discretized models, however more intricate three-dimension simulation of turbulent flow requires increasingly more degrees of freedom and create oversized data sets to be investigated. Design challenges such as optimization of rotor shape become impossible due to limits of CPU power and the necessity for smaller data sets, which leads to the introduction of reduced order models [Burkardt 2003, Lucia 2004].

In a URANS simulation on an S-duct and a single stage fan, it was shown that CPU run time approached 46 days on 4096 processors (4.5 million CPU hours) [List 2013]. As HPC systems have a finite number of processor availability, they are stretched to their limits with finely discretized URANS simulations.

Fast/ROM are characterized by the use of a reduced basis in place of state equations, which contain far fewer degrees of freedom compared to the complete discretized state equations. The basis $a_i, i = 1, \dots, n$ corresponds to the blade count and row, with the approximation $\tilde{a} = \sum_{i=1}^{n} M_i a_i \in V \equiv span\{a_1, \dots, a_n\} M$ coefficients correspond to spinning mode inputs to the HB simulation and V are spatial approximations [Burkardt 2003]. Here the state is reduced to the V lower dimension.

The HB fast method is a variation of a time-domain turbomachine analysis, which predicts essential flow features when compared to complete time-marched CFD and experimental solutions. As the flow in a fan stage is periodic from blade to blade, the basic governing Navier-Stokes (NS) equations are modeled in a reduced fashion in the frequency domain. The HB method utilized makes use of the frequency domain that negates the need for time-accurate integrations [He 2010].

2.2 Navier-Stokes Equations

CFD solves nonlinear partial differential equations that model the conservation of momentum, energy, and mass flow simultaneously. In addition, a turbulence model is often used. Mass and energy are both modeled by one conservation equation as they are scalar quantities. On the contrary, there are three momentum equations as momentum is a vector quantity and a different equation is required for each direction. As mass, momentum, and energy physically are conserved in all situations, a domain can be broken up into infinitesimally small grid blocks where the calculations are simplified from element to element but as a whole can predict fluid dynamics on a system level. This concept is the basis for CFD.

The partial differential equations are known as the Navier-Stokes equations and are the basis of fluid dynamics which can be used to model a wide variety of fluid problems ranging from blood flow, to buoyancy, to acoustics, to flow surrounding an aircraft to name a few. The fluid is assumed to be a homogenous continuum and isotropic [Kays 2004]. Derivations of these equations stem from applying Newton's second law of motion to fluids and realizing that tangential stress in the fluid is the sum of the diffusing viscous and pressure terms [Kays 2004].

An extra equation is used in the form of a turbulence model. As turbulence is present in the flow regime of this study, the Spalart-Allmaras turbulence model is a viable candidate for flow prediction. Two key assumptions are made in the derivation of the viscous fluid model:

- The viscous diffusion is proportional to the rate of strain.
- Stress is hydrostatic when the fluid is at rest. [Kays 2004]

2.2.1 Conservation of Mass

Conservation of mass or the continuity equation is the simplest of the five partial differential equations. There is no generation term in the equation. There is however a storage term. The mass that enters the control volume is either stored or exits. In its simplest form, the conservation of mass is:

$$\dot{m}_{in} - \dot{m}_{out} = \dot{m}_{stored} \tag{1}$$

In other terms, the fluid mass that enters the control volume minus the fluid mass that leaves the control volume must equal the stored fluid mass. From a differential basis, the governing continuity equation in Cartesian coordinates becomes

$$\frac{\partial \rho}{\partial t} + \frac{\partial (\rho v_x)}{\partial x} + \frac{\partial (\rho v_y)}{\partial y} + \frac{\partial (\rho v_z)}{\partial z} = 0 \tag{2}$$

The v stands for fluid velocity vector in its respective direction, where ρ is the fluid density. Mass flow is represented in the density term as density is simply the mass in a given volume [Kays 2004].

2.2.2 Conservation of Momentum

Momentum conservation is different from mass conservation in the fact that momentum acts as a vector rather than a scalar. This means each direction requires a different partial differential equation. These equations are commonly used in a Cartesian coordinate systems, but can easily be converted to cylindrical or spherical if the need arises.

$$P_{in} - P_{out} = P_{stored} + P_{generated} \tag{3}$$

Considering Newton's Second Law, an applied force is equal to mass times acceleration. Mass multiplied by acceleration is less commonly known as the first derivative of an object's momentum in the time domain. The law can be applied to homogenous fluids the same as a simple particle.

$$\vec{F} = m \times \vec{a} = \frac{d\vec{p}}{dt} \tag{4}$$

where *F* is the applied force, *m* is mass, *a* is acceleration, and *p* is linear momentum. The change of fluid momentum in the control volume occurs mainly due to the convective forces that drive the fluid motion. In the presence of a solid surface, viscous stresses between the wall and fluid arise and attribute to momentum change. Similarly, body forces such as gravitational pull affect momentum change [Kays 2004]. Adding these forces into the equations yields:

X-direction momentum:

$$\rho\left(\frac{\partial v_x}{\partial t} + v_x\frac{\partial v_x}{\partial x} + v_y\frac{\partial v_x}{\partial y} + v_z\frac{\partial v_x}{\partial z}\right) = -\frac{\partial P}{\partial x} + \rho g_x + \mu\left(\frac{\partial^2 v_x}{\partial x^2} + \frac{\partial^2 v_x}{\partial y^2} + \frac{\partial^2 v_x}{\partial z^2}\right) \tag{5}$$

Y-direction momentum:

$$\rho\left(\frac{\partial v_y}{\partial t}+v_x\frac{\partial v_y}{\partial x}+v_y\frac{\partial v_y}{\partial y}+v_z\frac{\partial v_y}{\partial z}\right)=-\frac{\partial P}{\partial y}+\rho g_y+\mu\left(\frac{\partial^2 v_y}{\partial x^2}+\frac{\partial^2 v_y}{\partial y^2}+\frac{\partial^2 v_y}{\partial z^2}\right) \quad 6)$$

Z-direction momentum:

$$\rho\left(\frac{\partial v_z}{\partial t}+v_x\frac{\partial v_z}{\partial x}+v_y\frac{\partial v_z}{\partial y}+v_z\frac{\partial v_z}{\partial z}\right)=-\frac{\partial P}{\partial z}+\rho g_z+\mu\left(\frac{\partial^2 v_z}{\partial x^2}+\frac{\partial^2 v_z}{\partial y^2}+\frac{\partial^2 v_z}{\partial z^2}\right) \quad 7)$$

where ρ stands for density, v stands for velocity in its respective direction, P is pressure, g is the acceleration due to gravitation, and μ is viscosity [Kays 2004].

2.2.3 Conservation of Energy

The conservation of energy equation comes from the first law of thermodynamics. The concept that must be understood to derive the equation is very similar to the mass and momentum conservation equations.

$$\dot{E}_{total}=\dot{E}_{in}-\dot{E}_{work} \quad 8)$$

E is the sum of kinetic, potential, and internal energy of the fluid. $\dot{E}_{total}$ refers to the total energy change of the system while $\dot{E}_{in}$ is energy transfer into the system and $\dot{E}_{work}$ is the work done by the system [Kays 2004]. The differential form of the energy equation is shown below, where Re_r is the Reynolds number, Pr_r is the Prandtl number, and τ represents shear stress.

$$\frac{\partial(E_t)}{\partial t} + v_x\frac{\partial(E_t)}{\partial x} + v_y\frac{\partial(E_t)}{\partial y} + v_z\frac{\partial(E_t)}{\partial z}$$
$$= -\frac{\partial(v_x p)}{\partial x} - \frac{\partial(v_y p)}{\partial y} - \frac{\partial(v_z p)}{\partial z} - \frac{1}{Re_r Pr_r}\left[\frac{\partial q_x}{\partial x} + \frac{\partial q_y}{\partial y} + \frac{\partial q_z}{\partial z}\right]$$
$$+ \frac{1}{Re_r}\left[\frac{\partial}{\partial x}\left(v_x\tau_{xx} + v_y\tau_{xy} + v_z\tau_{xz}\right)\right.$$
$$\left. + \frac{\partial}{\partial y}\left(v_x\tau_{xy} + v_y\tau_{yy} + v_z\tau_{yz}\right) + \frac{\partial}{\partial z}\left(v_x\tau_{xz} + v_y\tau_{yz} + v_z\tau_{zz}\right)\right] \quad (9)$$

2.2.4 Spalart-Allmaras Turbulence Model

The Spalart-Allmaras turbulence model solves a single transport equation that determines the kinetic energy turbulent viscosity [Deck 2001]. Designed for aerospace applications with high adverse pressure gradients, the Spalart-Allmaras model can be used in two or three dimensional CFD and does not require any specific grid density to produce accurate results. The Spalart-Allmaras model is given by

$$\frac{\partial\tilde{v}}{\partial t} + \tilde{u}_j\frac{\partial\tilde{v}}{\partial x_j} = \underbrace{c_{b1}\tilde{S}\tilde{v}}_{Production} + \underbrace{\frac{1}{\sigma}\left[\frac{\partial}{\partial x_j}\left((v+\tilde{v})\frac{\partial\tilde{v}}{\partial x_j}\right) + c_{b2}\frac{\partial\tilde{v}}{\partial x_j}\frac{\partial\tilde{v}}{\partial x_j}\right]}_{Diffusion} - \underbrace{c_{w1}f_w\left(\frac{\tilde{v}}{d}\right)^2}_{Destruction} \quad (10)$$

and directly solves a transport equation for eddy viscosity. Important terms are production, diffusion, and destruction. This model has proven reliable for transonic turbulent flow [Deck 2001], separated flow in nozzles [Deck 2001], and in supersonic configurations [Deck 2001].

2.3 Harmonic Balance Formulation

The HB technique allows for the calculation of unsteady flow features using a combination of frequency and time domain CFD methods. The solution is governed by the Navier-Stokes equations seen in Sections 2.2.1-2.2.4 and is a fast CFD method. The computational domain under consideration is first discretized using a finite volume scheme and second order accuracy with a combination of structured and unstructured elements as discussed in Section 3.2. The diffusion flux element is a second-order central difference. The convective flux is standard upwind, flux difference [Custer 2012].

The frequency and wavelengths of the unsteady disturbance are calculated with the blade count where for a two blade row rotor/stator configuration is given by

$$N = m_1 B_1 + m_2 B_2 \tag{11}$$

where m_1 and m_2 are indices and N represents the nodal diameter (proportional to wavelength) of the spinning mode. The frequencies of the stationary and rotating reference frames are then calculated by

$$\omega = m_2 B_2 \Omega \quad and \quad \omega = -(m_1 B_1)\Omega \tag{12}$$

The harmonic balance solver enables the use of pseudo-time marching methods to calculate an unsteady CFD solution using steady flow solver techniques [Custer 2012]. It accomplishes this by transforming the solution from the time domain to the frequency domain using a discrete Fourier transform. This frequency domain analysis first requires a steady solution. This is computed on the flow domain using conventional time-domain techniques and is represented in three dimensions by

$$w(x,y,z,t) = w_0(x,y,z,t) + \sum_{n=1}^{m} w_{2n-1}(x,y,z)\cos(\omega n t) + w_{2n}(x,y,z)\sin(\omega n t) \quad (13)$$

where x, y, z are Cartesian coordinates, t is time, t_k represents higher time levels, m is the number of harmonics, w_0 is the mean (steady state) solution at the location and time, w_n are the fourier coefficients, and ω is the excitation frequency of unsteady disturbance [CD-Adapco 2016]. Knowing that the unsteadiness is small and periodic (Eq. 14) in time, the fluid motion and boundary conditions are linearized about the steady solution resulting in harmonic coefficient equations (Eq. 15-17) that describe the small unsteady disturbances [Custer 2012]. The periodic properties are subsequently utilized in Eq. 18 to represent the full annulus solution at discrete time levels, k.

$$w_k^* = w(t = t_k) \quad (14)$$

$$t_k = \frac{2\pi k}{\omega N} \quad (15)$$

$$w_0 = \frac{1}{N}\sum_{k=0}^{N-1} w_k^* \quad (16)$$

$$w_{2n-1} = \frac{2}{N}\sum_{k=0}^{N} w_k^* cos\omega n t_k; n = 1 \dots m \quad (17)$$

$$w_k^* = w_0 + \sum_{n=1}^{m}[w_{2n-1}\cos\left(\frac{2\pi n k}{N}\right) + w_{2n}\sin\left(\frac{2\pi n k}{N}\right) \quad (18)$$

Next, taking the time derivative of w_k^* at each time level and substituting Eq. 15-17 into Eq. 18 gives

$$\frac{\partial w_k^*}{\partial t} = \frac{2\omega}{N}\sum_{n=1}^{m} n[\cos\left(\frac{2\pi nk}{N}\right)\sum_{j=0}^{N-1} w_k^* \sin\left(\frac{2\pi nj}{N}\right) - \sin\left(\frac{2\pi nk}{N}\right)\sum_{j=0}^{N-1} w_k^* \cos\left(\frac{2\pi nj}{N}\right) \quad (19)$$

Finally, Eq. 21 is representative of a vector of time derivatives with an Euler implicit discretization and transform operator *D*, used as the time derivative source term in the conservation equations. [CD-Adapco 2016] *D* is the *N*x*N* pseudo-spectral matrix operator, and the flux vectors are evaluated using the matching time level solution and links all time levels [Custer 2012]. The coupled solver transforms from Eq. 20 to the HB equation given by Eq. 21.

$$\oint [F - G] \cdot d\tilde{a} = \int_{\tilde{V}} H d\tilde{V} - \frac{\partial}{\partial t}\int_{\tilde{V}} W d\tilde{V} \quad (20)$$

$$\oint [F^* - G^*] \cdot da = \int_V H^* dV - \int_V DW^* dV \quad (21)$$

2.4 Harmonic Balance Limitations

The computationally efficient, harmonic balance CFD method can compute unsteady flow solutions only for temporally periodic situations; meaning that it is best suited for turbomachinery and rotorcraft applications involving, for instance, tonal aeroacoustics, forced response, and flutter calculations. Harmonic balance cannot be applied to transient problems that are non-periodic in time. Furthermore, the Fourier transform nature of the HB method requires a temporally constant inlet distortion boundary condition (in the stationary frame of reference).

2.5 Harmonic Balance Accuracy

The accuracy of STAR-CCM+ software, and specifically HB has been shown in various studies. In a URANS simulation of an S-duct geometry, an 8% difference was found between experimental and URANS flow variable values [Sanders 2013]. In a study completed by Peterson, URANS and HB simulations were compared in an effort to quantify solution differences [Peterson 2015].

The Peterson study used the rotor 4 geometry and STAR-CCM+ URANS and HB methods. A 90º sector inlet distortion was applied as an upstream forcing function. The difference in performance values of URANS and HB methods are shown in Table 1 and show percent changes consistently less than 1%. These low percent differences validate the HB solver in capturing flow physics under the application of a total pressure distortion [Peterson 2015].

It should be noted, the spinning mode index combinations used in the Peterson study, (5, 0, 0), (3, 1, 1), and (2, 2, 2), are not the same as the ones used in the parametric study of this thesis. Explanation of the user-defined spinning mode is found in Section 4.3.2.

Table 1. Percent Difference of HB Solutions compared to URANS

	HB (5, 0, 0)	**HB (3, 1, 1)**	**HB (2, 2, 2)**
Inlet Total Pressure	0.6%	0.6%	0.5%
Inlet Total Temperature	0.0%	0.0%	0.0%
Exit Total Pressure	0.3%	0.1%	0.2%
Exit Total Temperature	0.1%	0.1%	0.0%
Total Pressure Ratio	0.9%	0.5%	0.3%
Total Temperature Ratio	0.1%	0.0%	0.0%
Efficiency	1.8%	1.0%	0.7%

[Peterson 2015]

2.6 Inlet Distortion Boundary Conditions

The SAE industry standard categorizes inlet distortion types as stagnation pressure, stagnation temperature, swirl (circumferential flow), and planar waves [SAE 2013]. Swirl is further categorized as bulk, tightly-wound, paired, and cross-flow [SAE 2010]. Any combination of these types may occur in an engine inlet flow. In this research, a paired-swirl inlet flow field is parameterized by retaining constant temperature and pressure profiles while varying velocity directional components in increasing swirl cases.

3. SIMULATION COMPONENTS

3.1 Test Article

The computational model is based on a transonic fan stage with a 17-inch tip diameter. The rotor is a diffusion-controlled airfoil design. At design speed, the rotor turns at 20,200 rpm and displaces approximately 60.8 lbm/sec of air with a stage pressure ratio of 1.92. This equates to a blade tip speed of 1500 ft/s, and the rotor exhibits supersonic Mach numbers on over 60% of the blade. The first region of the model was located from the AIP to just upstream of the rotor stage and was a moving reference frame.

As this is a single stage fan, a nose cone structure (or spinner) is upstream of the rotor blades, and further upstream is the inlet boundary at which the inlet distortion boundary conditions were applied, designated the aerodynamic interface plane. The solution domain extends downstream to the station designated the dump plenum plane. Flow is from left to right in the axial view of Figures 2 and 3. Figure 3 shows the entire flow domain that the HB technique simulates using the calculations of a single representative sector and Fourier transforms. The HB computational technique allowed for the single sector model to represent the entire annulus.

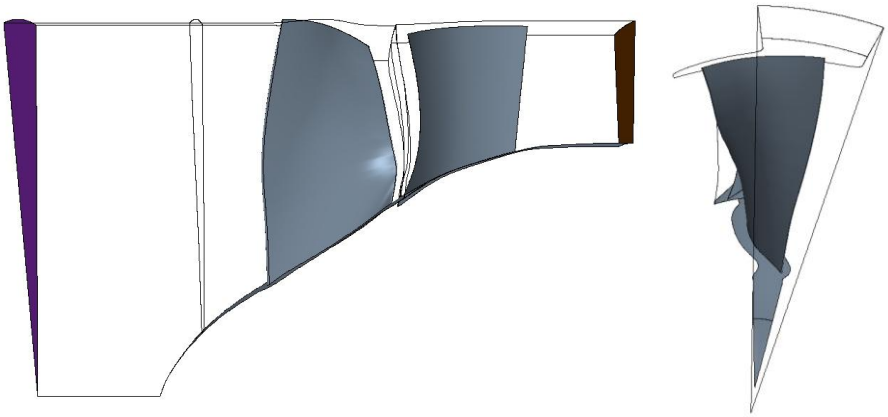

Figure 2 - Single sector axial and tangential views of rotor/stator geometry and computational domain used in the CFD processing.

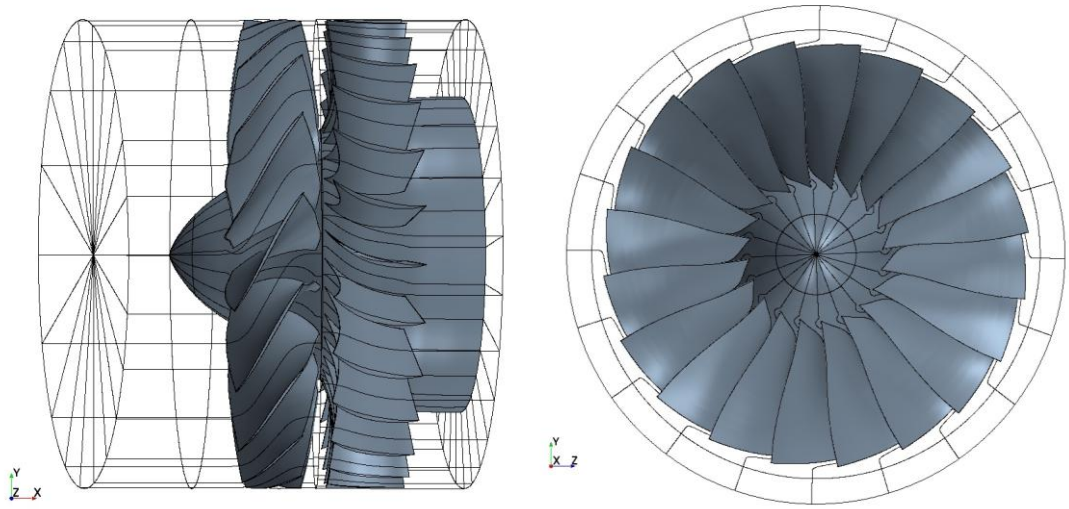

Figure 3 – The harmonic balance solution calculated on a single blade passage domain represents, through series expansion, the entire annular flow domain, allowing for application of even low engine order inlet distortions to the aerodynamic inlet plane.

Table 2. Fan Stage Specifications

Design Parameter	Value
Rotor Blades	20
Stator Blades	31
Tip Clearance	0.020-0.025 in
Flow Rate	60.77 lbm/s
Rotational Speed	20,200 rpm
Pressure Ratio	2.057
Efficiency	94.60%

3.2 Meshes

The CFD model is made up of a combination of structured and unstructured elements for the inlet distortion simulations. Non-reflective boundary conditions were applied on the inlet/exit and mixing plane boundaries to prevent the reflection of the upstream propagation waves back into the flow domain and to diminish numerical reverberation of artificial reflections. Because a portion of the rotor sector domain, upstream of the nose cone, includes the axis of rotation, the domain terminates along the centerline of the model, Figure 2. Here STAR-CCM+'s polyhedral

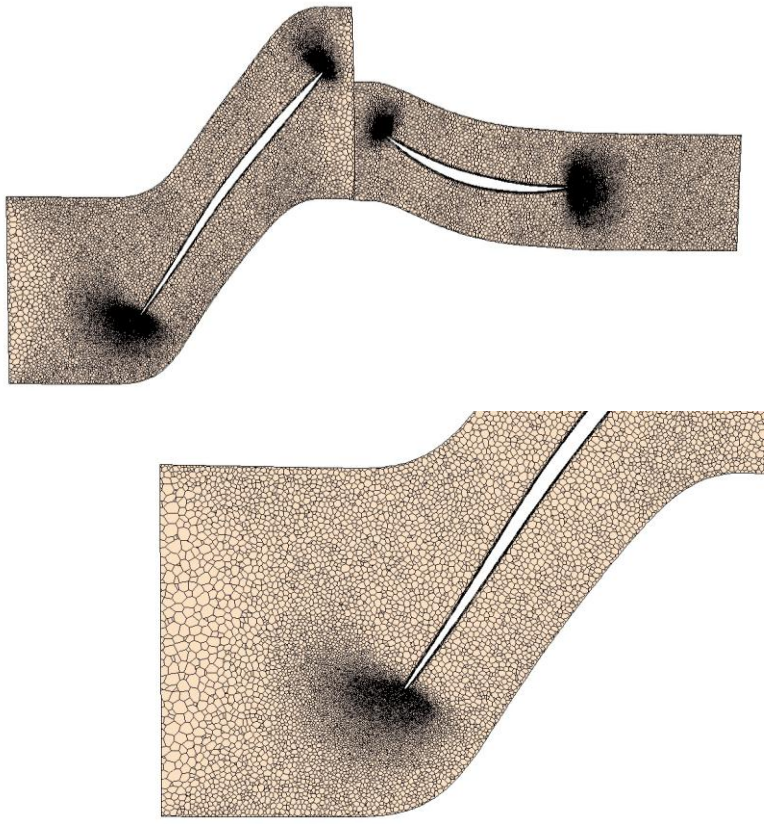

Figure 4 - Original polyhedral meshing technique that proved unusable for harmonic balance simulations because of a zero radius point at the centerline upstream of the rotor leading edge (not shown).

meshing technique, Figure 4, could not discretize the region upstream of the nose cone adequately.

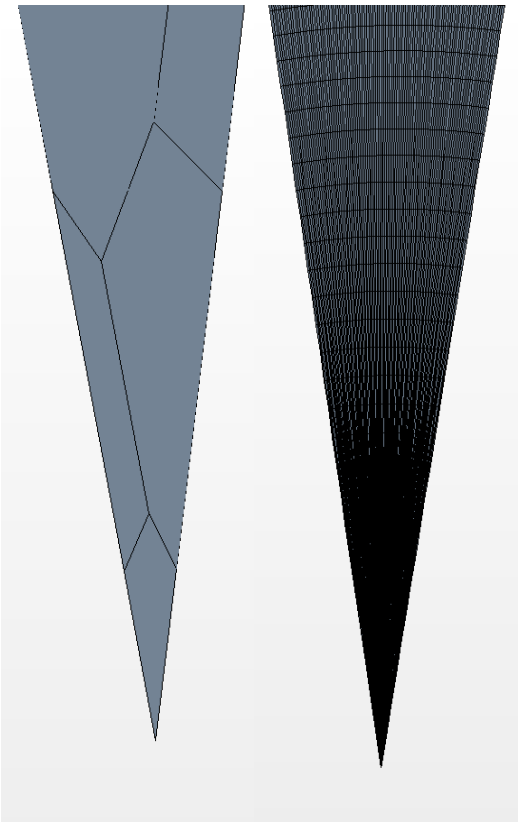

Figure 5 - Polyhedral vs. structured mesh in the tangential direction at the hub centerline.

The polyhedral mesh generation algorithm produced single cells in the tangential direction and therefore lacked the number of cells to satisfy the spatial Nyquist criteria required for HB non-reflective boundaries. The number of cells in the tangential direction is required to be greater than two times the number of desired non-reflecting boundary condition modes plus one. Figure 5 shows an unusable mesh with one cell at the hub versus a usable mesh, which meets the Nyquist criteria.

$$\text{Number of tangential cells} > 2n+1$$

$$n = \text{boundary condition modes} \qquad 22)$$

Implementing a structured and polyhedral combination mesh in the rotor region allowed for control of the number of cells in the tangential direction but also kept the amorphous polyhedral benefits near the rotor surface. This is expected to be beneficial when simulating blade motion as the cells can move more freely with the blade surface (not implemented in this study).

The mesh generated for the fan calculations was composed of approximately 14.9 million cells. The computational mesh in the rotor and stator regions included 11.9 and 3.0 million cells, respectively. Prism layers were generated on all physical surfaces including the blades, shroud, and hub with the goal of satisfying proper y^+ conditions. Furthermore, no refinement was added as the regions were sufficiently dense with a uniform mesh. Note that the curved lines on the structured mesh displayed in Figure 6 have no physical meaning, as they are simply aliasing with

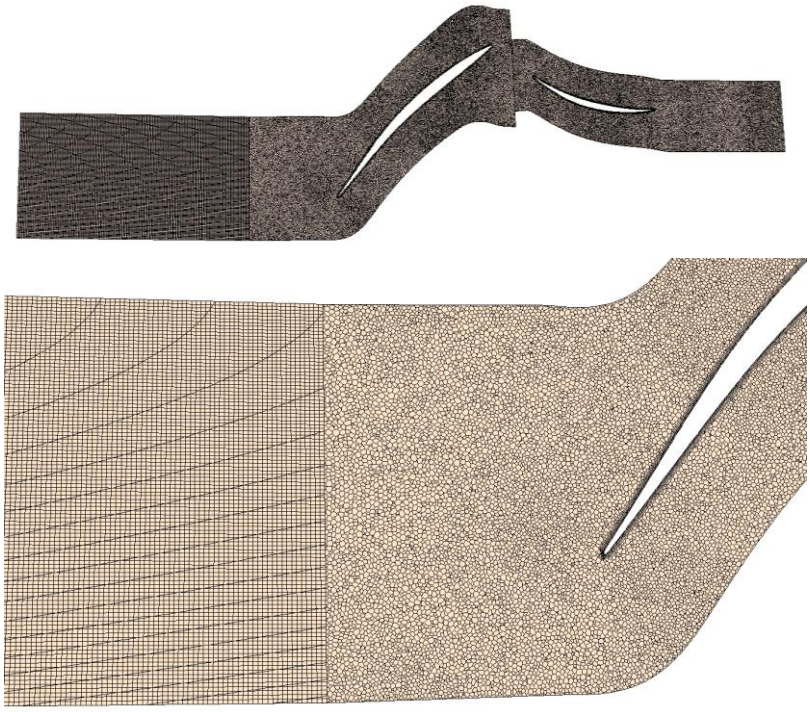

Figure 6 - Slice at 90% span showing the combination structured/polyhedral meshing technique used to satisfy Fourier transform criteria at the rotor center line.

the computer screen resolution.

The polyhedral mesh was useful in that the amorphous pattern made the mesh less sensitive to the effect of mesh stretching and gave each cell more points for computation than the traditional brick method. One downside to this method was the increase of computational

expense per element. The following mesh models were selected and generated by choosing a base cell size and using functions available in STAR-CCM+:

- Polyhedral elements (however in-house meshing software was used for the region upstream of the cone to produce hexahedral elements)
- Prism layers
- Surface re-mesher

Prism layers were not present on boundaries that were not physical surfaces, as the solution diverged if a prism layer was generated on any other of the boundaries, such as the inlet, outlet, mixing planes, and periodic planes. While turning the prism layers function on automatically generates prisms on all boundaries, they were subsequently turned off.

In addition, changing the mesh with surface curvature specification is unadvised due to the lack of mesh quality improvement for the addition of cells and CPU time. The mesh size nearly exponentially increased with the increase of the surface curvature expansion without improving the flow prediction for the entire region. Surface curvature only affected regions near the leading and trailing edge of the blade. These grid generation steps were imperative to completing a successful mesh convergence study (see section 4.3.1).

When using periodic boundaries, the angle of rotation is not identified until the region is meshed. A single hidden check box must be ticked prior to the meshing sequence in order to detect the angle of rotation of the region. Prior to meshing, the periodicity was set to rotational, and the locked angle function was unchecked.

Regions where the polyhedral cell technique is poor, a structured mesh can be implemented. A brick mesh was generated using an in-house meshing code and imported to

match the model geometry. An internal interface between the polyhedral and structured mesh was implemented, ensuring proper communication between the two meshes.

3.3 Computer System Specifications

The computations were executed on the AFRL DSRC supercomputer at Wright-Patterson AFB while pre- and post-processing tasks were completed on the Enclave cluster administered by AFRL RQT. These computer systems are advanced and capable of handling large computing jobs. The DSRC supercomputer has 2.6 GHz Intel E5 Sandy Bridge Core with 4,590 compute nodes and makes use of an allocation scheduling system. Sixty nodes with 16 processors per node and 32 Gbytes of memory per node were utilized for the computation of the parametric study simulations presented in the results section.

All simulations were completed using STAR-CCM+ Version 10.04.009. Steady state simulations made use of second-order spatial accurate calculations while HB simulations made use of first-order spatial accurate calculations.

3.4 Discretization

The solver in STAR-CCM+ uses an unstructured mesh, finite volume, computational method with various schemes and orders of accuracy. As the mesh is in the form of polyhedral cells, the conservation equation variables are calculated at the cell nodes and integrated to approximate the cell center values. The simulations seen in this thesis used a second-order upwind scheme for the steady-state analysis and a first-order upwind scheme for the HB parametric study [CD-Adapco 2016].

The second-order scheme is preferable with its increased accuracy due to limited truncation error as compared to the first-order scheme. However, first order schemes allow for faster, more stable computation. Trial and error proved that the second-order scheme was unstable for the flow simulated in this study, resulting in poor convergence for any simulation using the HB solver even with a minimal CFL. Therefore, the steady-state flow field was analyzed using a second-order simulation which was then changed to first order for the HB calculations.

4. METHODOLOGY

4.1 Inlet Distortion Description

The baseline inlet distortion of this study is consistent with that of a homeomorphic variant of the M2129 duct. The M2129 duct, Fig. 8, produces a separation region, Fig. 9, which in turn yields a stagnation pressure variation and twin swirl at its exit plane, Fig. 10. These predictions are from a STAR-CCM+ model of the M2129 duct. The predictions of Figs. 9 and 10 were generated through CFD simulation using STAR-CCM+. An M2129 S-duct model, Figures 7 and 8, was scaled to the 17 inch diameter of the fan model. A favorable pressure gradient from the inlet to the outlet drove the flow. The total-to-total is pressure ratio is 0.952 causing the mass flow rate of the duct to match fan design point mass flow. It was discretized into a mesh of approximately 526,000 elements and the following physics models were applied:

- All y+ wall treatment
- Coupled Energy
- Coupled Flow
- Ideal Gas
- Implicit Unsteady
- RANS
- SST K-Omega Turbulence

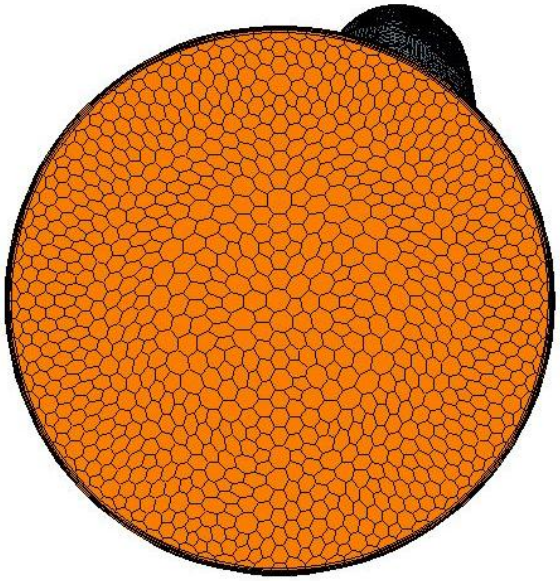

Figure 7 - M2129 meshed AIP surface.

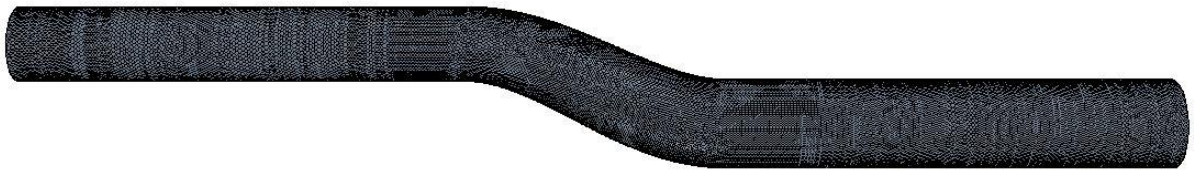

Figure 8 - M2129 S-duct geometry and axial meshing.

Upon convergence, the model exhibited a mass flow of 60.7 lbm/s and a distortion pattern similar to research by Mohler [Mohler 2004]. The model solution showed separation of flow along the lower surface of the M2129 S-duct. This separation in turn caused a distortion pattern to propagate downstream. By the time the distortion reached the exit, vorticity was significant while pressure and temperature gradients manifested. Typical time domain solutions are shown in Figures 9 through 10.

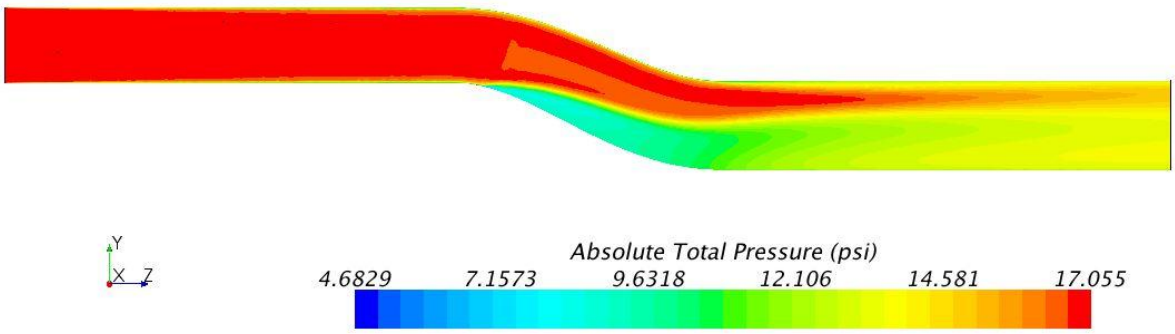

Figure 9 - Absolute total pressure through the M2129 S-duct axial view. Note the low pressure separation on the lower surface at the curve.

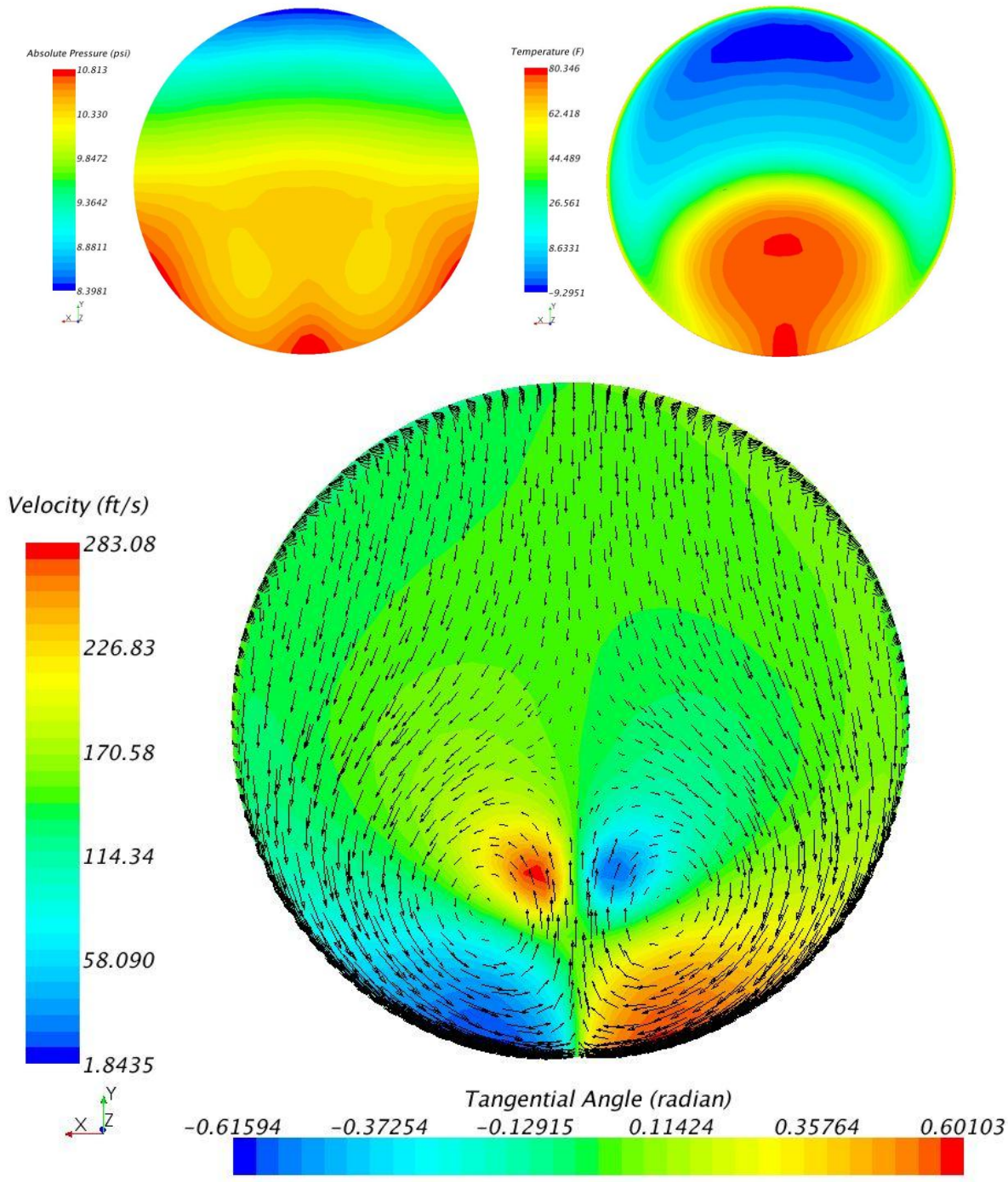

Figure 10 - Predicted M2129 duct exit patterns. Top Left: absolute pressure distortion pattern. Top Right temperature distribution. Bottom: Velocity distortion pattern.

4.2 Inlet Distortion Parametric Formulation

A parameterization method was formulated with the general goal to preserve the inlet distortion flow of a baseline flow, yet allow the study of the impact of the level of swirl. To accomplish this goal, a parameter was defined that conserved the flow kinetic energy at the inlet, but re-apportioned its balance of the axial and swirl (i.e., tangential and radial) constituents. Because the kinetic energy is conserved as the parameter is varied, the baseline stagnation and static properties of temperature and pressure are preserved. Furthermore, the in-plane velocity vector field shape is preserved, while its vector magnitudes are linearly scaled by the parameter. This is analogous to the scaling of an eigenvector.

The swirl parameter, *a*, was defined as follows. The axial, tangential, and radial velocity components that were specified as inlet boundary conditions in the computational model are *U*, *V*, and *W*. The velocity direction vectors are extracted from these components by the STAR-CCM+ software algorthm. The baseline values are denoted by the *b* subscript. Let

$$U = \sqrt{U_b^2 + (1 - a^2)(V_b^2 + W_b^2)} \tag{23}$$

$$V = aV_b \tag{24}$$

$$W = aW_b \tag{25}$$

$$a \geq 0 \tag{26}$$

$$Q_b^2 \stackrel{\text{def}}{\equiv} U_b^2 + V_b^2 + W_b^2 \tag{27}$$

By this formulation, the constraint that $Q_b^2 = U^2 + V^2 + W^2$ is enforced at each location on the AIP as the parameter was varied, and the baseline stagnation, static pressure and temperature on the AIP were preserved. Furthermore, the in-plane velocity vector field shape was preserved, while its vector magnitudes were linearly scaled by the parameter.

For simulation, the inlet boundary condition was applied to the AIP using the "spatial annular wake" specification in STAR-CCM+. The wake was specified on 31 concentric circles of the inlet with 73 points per circle. In addition, the simulations were completed retaining (6, 3, 0) spinning modes so as to capture the highest energy harmonics from the distortion, while avoiding stator forcing function unsteadiness. Such a setup allowed for identifiable inlet distortion effects on downstream flow physics and blade force measurements.

Though inlet kinetic energy, pressure, and temperature were conserved, the mass flow rate changed slightly, while pressure ratio was held constant. Redistributing kinetic energy from the axial velocity to the radial and tangential components yielded a deficit of inlet mass flow for higher swirl cases. The percent change of the mass flow rate are found in Table 3. The maximum deficit is shown in the maximum swirl case and proves to be less than a tenth of a percent off from the design mass flow rate of the no swirl case. This is assumed to have negligible effect on the parametric study results.

Table 3. Mass Flow Rate Change Between Parametric Cases

Case	Mass Flow Rate (lbm/s)	Percent Difference
a=0.0	60.70	0.00
a=0.5	60.69	-0.02
a=1.0	60.67	-0.05
a=1.5	60.65	-0.07

4.3 Solution Sensitivity Studies

4.3.1 Mesh Sensitivity

The mesh sensitivity study made use of a baseline mesh density of 14.9 million cells and the meshing shown in Figure 6. The baseline computational mesh in the rotor and stator regions included 11.9 and 3.0 million cells, respectively. The baseline mesh density was then bracketed ±20% with cell counts of approximately 12 and 18 million. All mesh sensitivity simulations were completed with no inlet distortion and 3 modes on both regions, meaning the user-defined

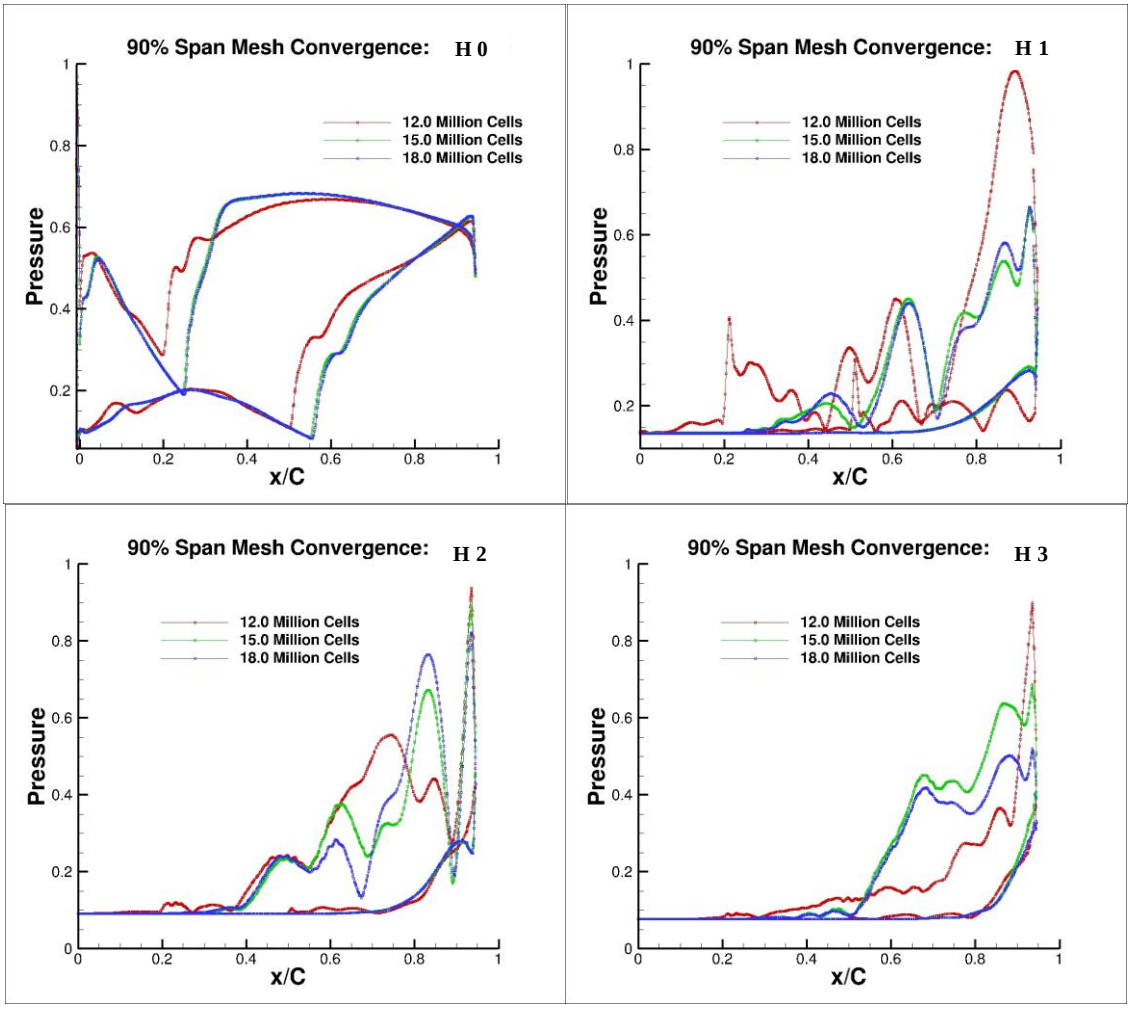

Figure 11 - Mesh Sensitivity Study. a: harmonic 0 b: harmonic 1 c: harmonic 2 d: harmonic 3.

harmonics for (inlet, rotor region, stator region) were (0, 3, 3). Harmonic pressures 0 through 3 were taken at 90% span on the rotor and subsequently plotted for the three mesh densities. The results show that for harmonics 0 through 3, the 14.9 and 18 million element mesh densities approach a single solution, while the 12 million element solution has not yet converged. Furthermore, the passage shock location depicted in the 0^{th} harmonic has converged to as single location. Similarly, the unsteady regions in the 1st and 2nd harmonics for the two higher mesh densities are convergent.

Integrated forces on the blade were used to compare quality of the mesh sensitivity simulations throughout all available harmonics. The most accurate case (18 million elements) was used as a reference to which the lesser cell count simulations were compared. Integrated forces show small discrepancies (≈3%) between the 15 and 18 million count simulations while the 12 million cell count simulation shows as high as a 16% difference. Therefore based on this mesh sensitivity study, the 14.9 million element mesh is used for all the results presented in the rest of this thesis.

Table 4. Mesh Sensitivity Integrated Force Percent Difference

Harmonic	**0**	**1**	**2**	**3**
12 Million	3.05%	16.12%	4.11%	13.09%
15 Million	0.35%	3.10%	0.56%	2.17%
18 Million	0.00%	0.00%	0.00%	0.00%

4.3.2 Spinning Mode Sensitivity

The modal sensitivity study consisted of four separate simulations having no applied inlet distortion. These simulations used the baseline mesh density, but with the spinning mode index limits (M_I, M_R, M_S) varied as (0, 2, 2), (0, 3, 3), (0, 4, 4), and (0, 5, 5). Running the simulations with high index limits is desirable to improve solution fidelity, however, computation time likewise increases. Each unique (*i, j, k*) triplet in the following equation corresponds to a spinning mode entered into the solution basis and increases the computational run time

$$iN_I + jN_R + kN_S = N \tag{28}$$

for $i \in [-M_I, M_I]$, $j \in [-M_R, M_R], k \in [-M_S, M_S]$. The spinning mode's nodal diameter, *N*, is built from a basis of fundamental nodal diameters corresponding to the inlet, rotor, and stator regions. For this thesis, the fundamental nodal diameters were set to unity, the rotor blade count, and the stator blade count, i.e. $N_I = 1, N_R = 20, N_S = 31$.

For the four simulations in Figure 12a, for the zeroth harmonic (i.e., time-mean) the variation of force magnitude acting on the blade changes 0.75%; for harmonic 1, 8.16%.

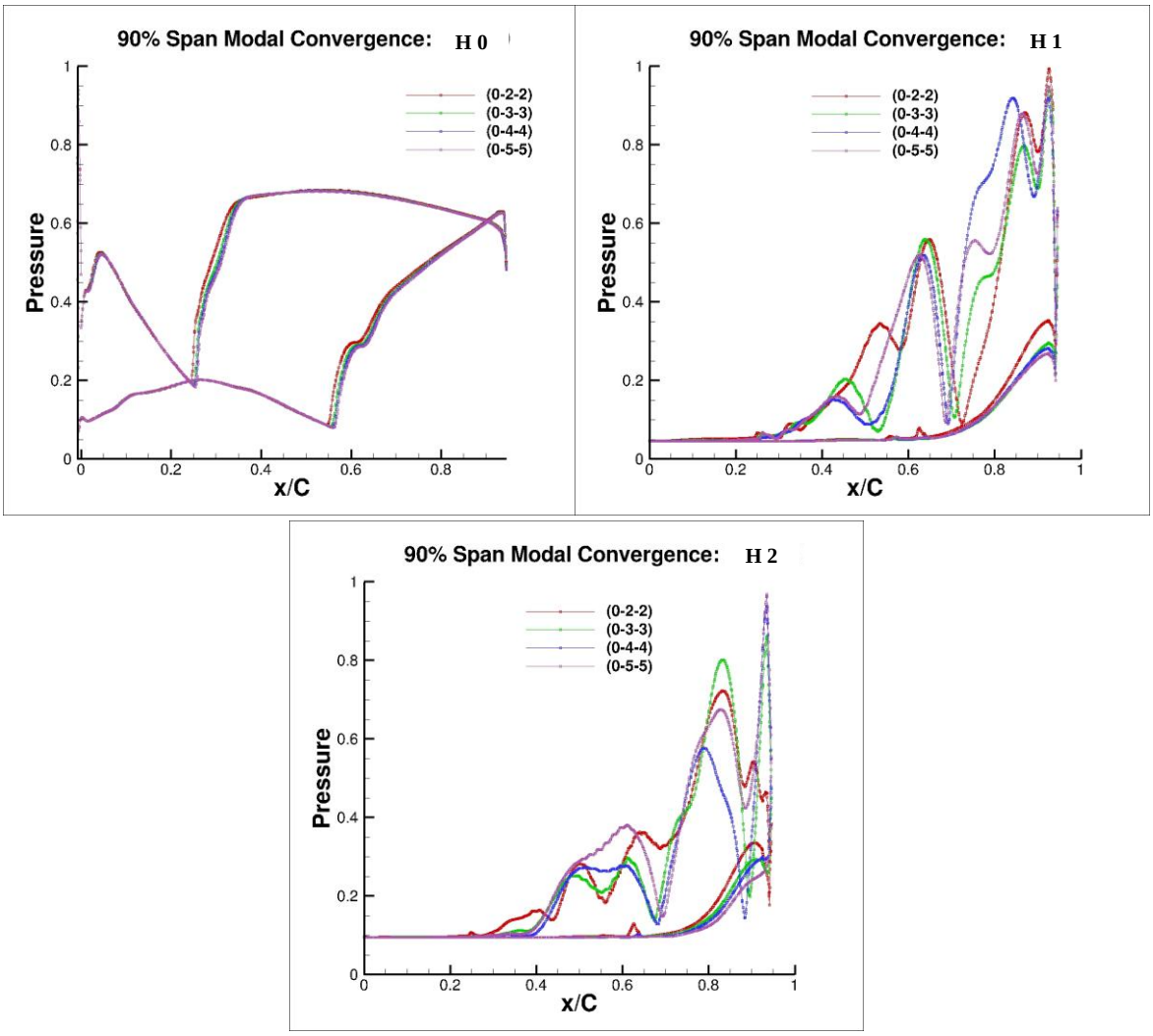

Figure 12 - Modal Sensitivity Study.

Table 5. Spinning Mode Sensitivity
Integrated Force Percent Difference

Harmonic	0	1	2
(0, 2, 2)	-0.75%	8.16%	-15.07%
(0, 3, 3)	-0.30%	-3.15%	-2.54%
(0, 4, 4)	-0.12%	-7.31%	-5.59%
(0, 5, 5)	0.00%	0.00%	0.00%

Upon investigation of the lower Fourier harmonics of the baseline inlet distortion, the most significant energy occurs in the first six harmonics, Figures 13 and 14. Therefore, six spinning modes were retained on the AIP spatial annular wake for the duration of the parametric study, ensuring unsteady energy capture. Similarly, during the parametric study, the number of retained spinning modes originating from the stator region was set to 0, so as to isolate the effects of the inlet distortion on the rotor blades. The spinning mode triplet was therefore applied as a (6, 3, 0) basis for all parametric simulations. In other words, the spinning mode triplet index limits (M_I, M_R, M_S) were set to (6, 3, 0), which allow the most energetic frequencies of the inlet distortion and rotor to be captured, while treating the stator region as a time-mean field providing economic savings in computation cost.

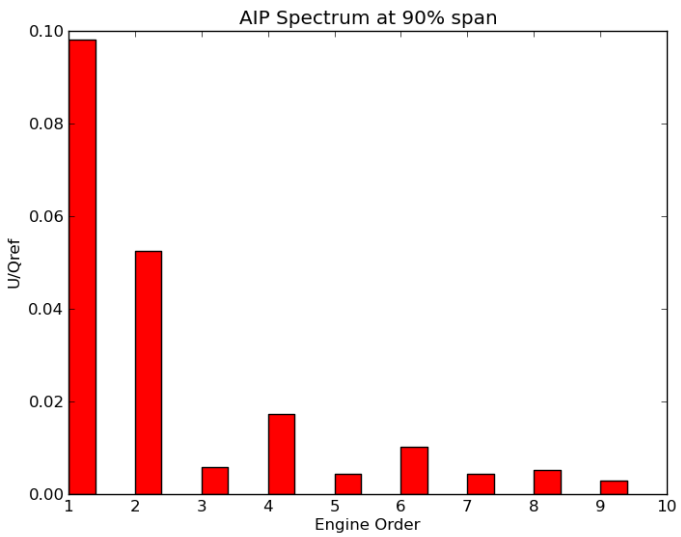

Figure 13 - Fourier spectrum of axial velocity of the baseline inlet distortion at 90 percent span.

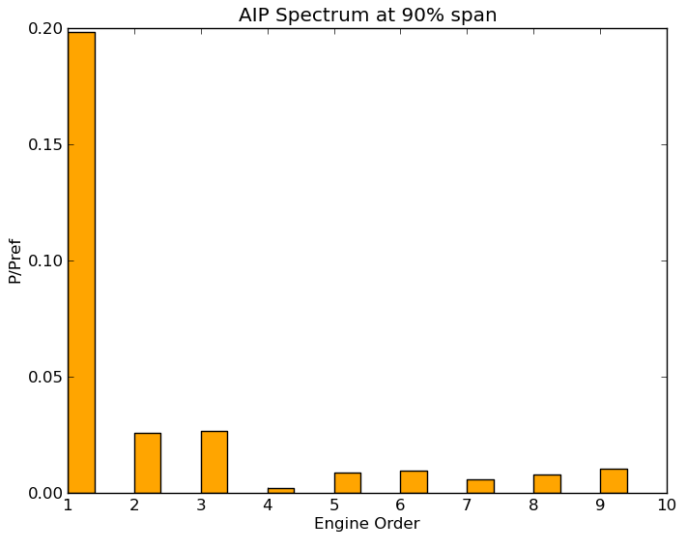

Figure 14 - Fourier spectrum of the pressure of the baseline inlet distortion at 90 percent span.

4.4 Numerical Convergence

4.4.1 Simulation Times

Simulation times depended greatly on the number of spinning modes applied to the regions. All simulation times can be found in Appendix A. In general, the (6, 3, 0) distortion parametric study simulations took between 20,000 and 21,000 CPU hours. Of the CPU hours, the steady state convergence took approximately ¼ of the time while the HB convergence took ¾. The sensitivity studies took between 6,000 and 15,000 CPU hours depending on the size of the mesh and spinning mode triplet.

4.4.2 Residual Plots

Residual plots are found in Appendix C. Simulations show convergence of 4 to 5 magnitudes. It was found that in all simulations, a minimum residual magnitude was reached after approximately 6,000 HB iterations. The residuals would subsequently grow slowly in magnitude for the remainder of computation.

The residual plots depict steady state simulations in which the pressure ratio was varied until it reached near design value. The desired pressure ratio of 1.92 was reached after 29,000 iterations. The HB physics continuum was then iterated for 6,000-7,000 iterations, or until pressure ratio and residuals had leveled out after the continuum change spike.

4.5 Steady-State Results

As noted previously, the harmonic balance distortion simulations required a converged steady state solution as a starting point. The setup for the steady state simulation can be found in Appendix B1. Convergence was monitored through the use of residual, pressure ratio, and mass flow plots. Residuals in Appendix C show two significant sections of convergence. From iterations 1 to 10,000, the simulation was converged to 4 magnitudes using no non-reflecting boundary conditions. From iterations 10,001 to 23,000, the simulation was converged to 4 magnitudes with non-reflecting boundary conditions on.

As well as using residual plots, mass flow and pressure ratio depict acceptable convergence for a steady state run. These plots can be seen in Appendix D. The plots not only show convergence when the change from iteration to iteration is small, but also ensured the simulation was on design conditions. For instance, the mass flow rate through the inlet sector model was 3.04 lbm/s. As the sector model was $1/20^{th}$ of the full annulus, it is seen that the mass

flow rate through the full annulus was 60.8 lbm/s. This is a 0.66% difference from the measured value of 60.4 lbm/s and ensures the simulation setup was done correctly.

4.6 Campbell Diagram and Blade Vibrational Mode Shapes

At design point, the fan turns 20,200 RPM and its forced response vibration susceptibility was inspected over its rotational speed range. The Campbell diagram, Figure 15, superimposes the blade natural frequencies for the first three vibrational modes (approximately horizontal curves) upon lines (spokes) that represent possible forcing frequencies for the lowest order harmonics of the inlet flow distortion. At the intersections of these curves, forced resonance is possible.

Figure 15 shows vertical, green dashed lines at fan idle and design speed. The crossings that occur near the design speed line are of most concern because of the high flow and forcing energy there. Consequently, particular attention is paid to the 2H, 5H, and 6H harmonics of the HB CFD simulation to assess the strength of forcing applied to the 1B, 2B, and 1T blade vibrational modes.

Figure 15 shows first bending (1B), second bending (2B), and first torsional (1T) mode shapes of the fan blade and are presented as unwrapped suction and pressure surfaces.

These mode shapes were calculated via ANSYS structural solver using a sector model of the bladed disk. Because the blade-to-air density ratio is large, these mode shapes are expected to remain unchanged with the introduction of the unsteady forcing function caused by the inlet flow distortion.

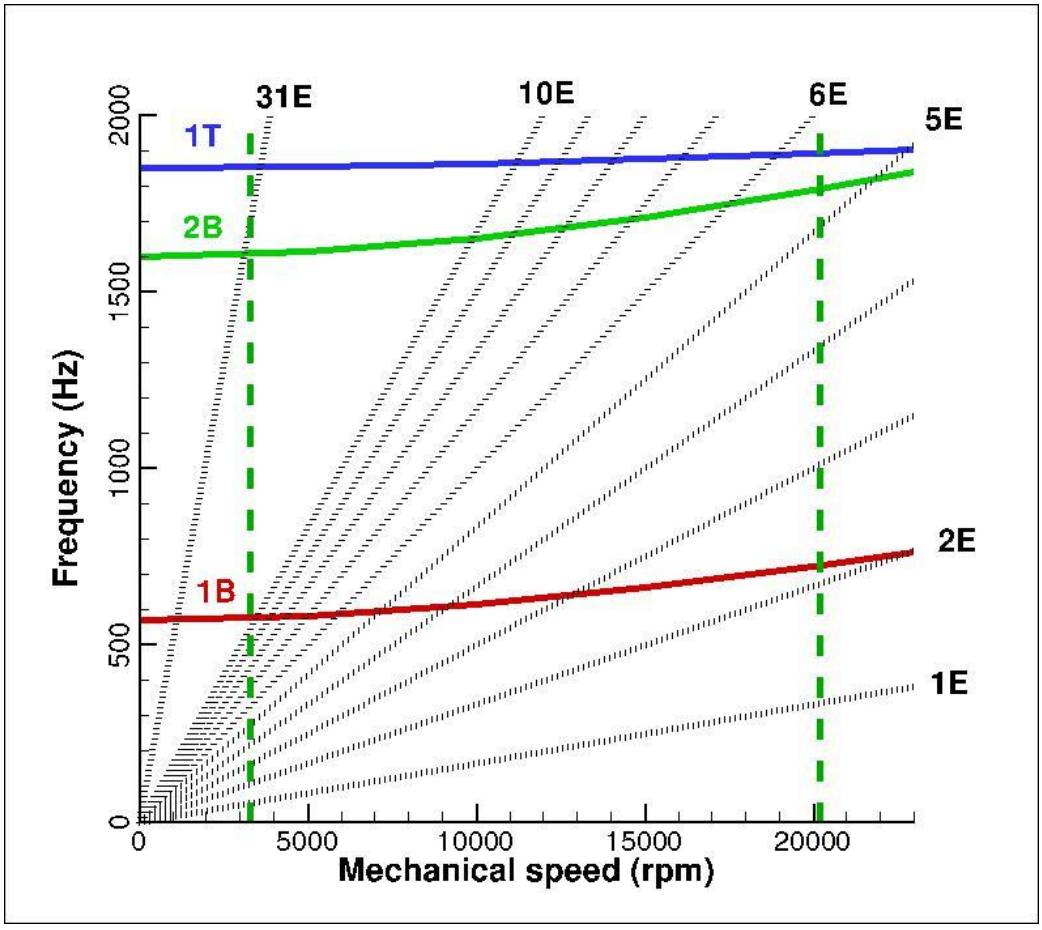

Figure 15 - Rotor 4 Campbell diagram showing the resonant frequencies.

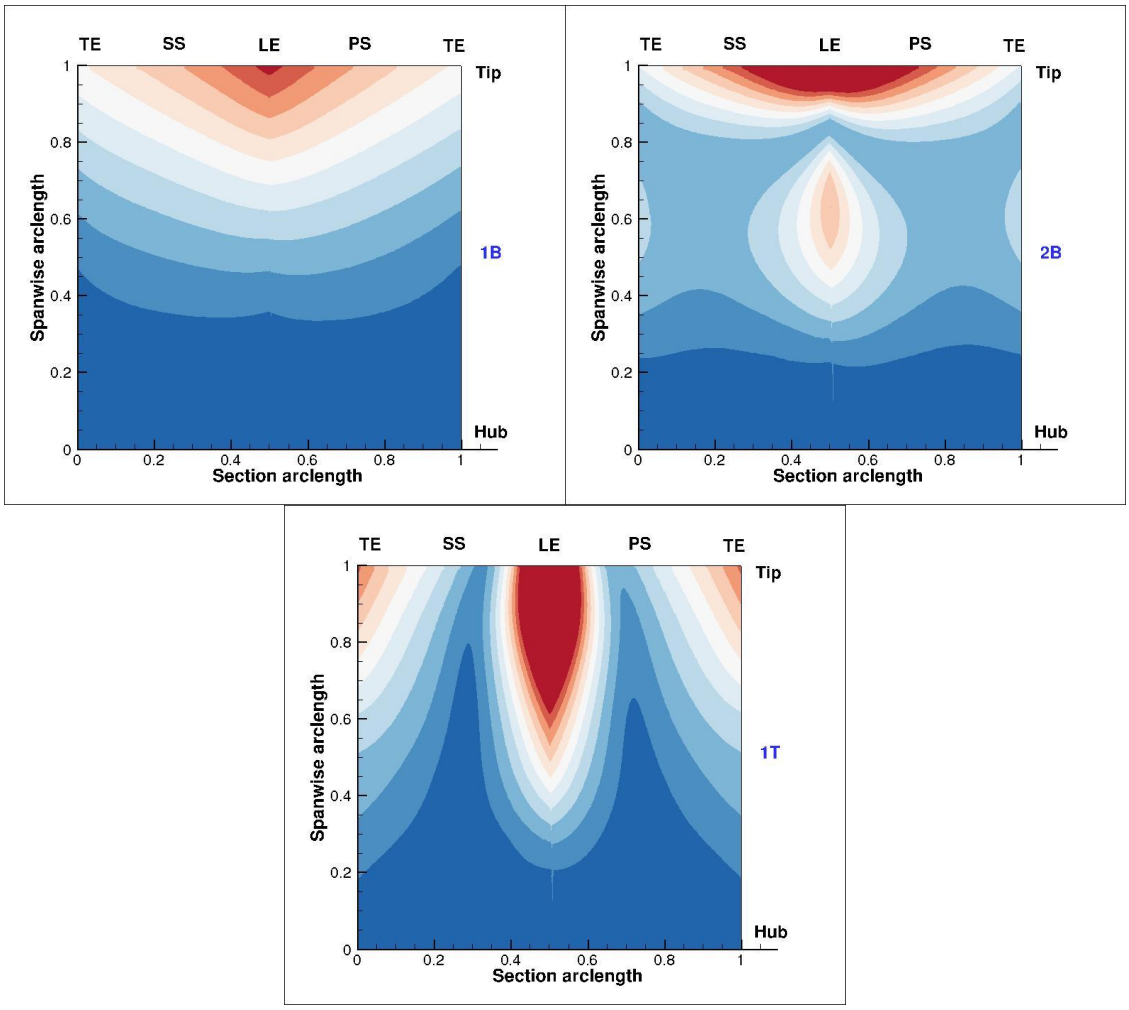

Figure 16 - Suction surface and pressure surface of the first and second bending and the first torsional vibrational modes of rotor 4.

4.7 Characterizing Inlet Distortion by Forcing Function Spectra

The harmonic content of an inlet distortion directly affects which blade vibrational mode shapes are excited, as correlated against the Campbell diagram. The harmonic content of the forcing functions associated with the inlet flow distortions used in this study are shown in Figures 17 through 20. The plots show engine order versus the radial location (zero being the

axis of rotation and one being the case wall). The size and hue of the circular symbol then represents the magnitude of harmonic content of the baseline inlet distortion pattern. A large, dark circle reveals higher harmonic content at the given location, while a small, pale circle reveals lower harmonic content.

The pressure, axial, and tangential velocity spectra are dominated by the first engine order. The radial velocity spectrum indicates significant energies in several lower engine orders.

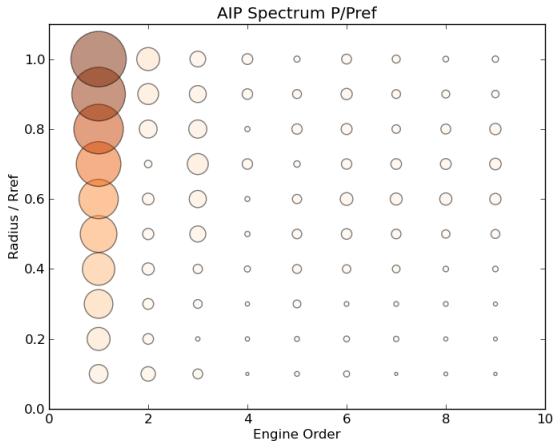

Figure 17 - Pressure spectrum.

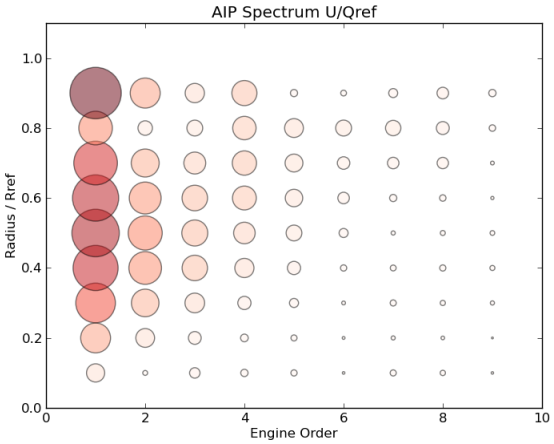

Figure 18 - Axial Velocity spectrum.

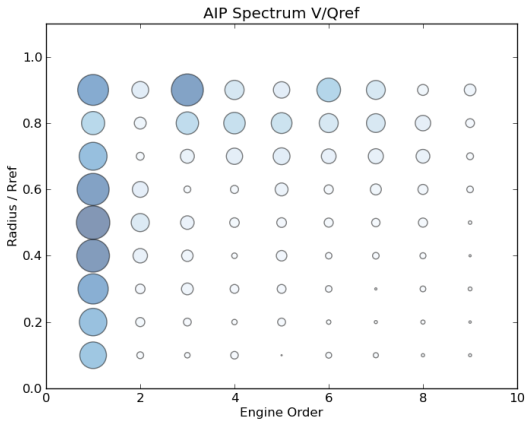

Figure 19 - Tangential velocity spectrum.

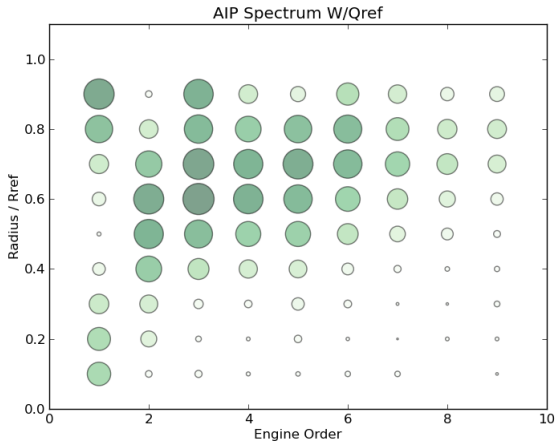

Figure 20 - Radial velocity spectrum.

5. DISTORTION PARAMETRIC STUDY RESULTS

5.1 Time Domain Flow Structure

The flow physics through the full annulus region was investigated on a 90% span cylindrical section though the annulus. Obvious changes in flow variables are compared with the varying applied inlet distortions. Four simulations with varying inlet distortion intensity were under consideration and the two extreme cases, a = 0.0 (zero swirl) and a = 1.5 (max swirl) are compared in the sections 5.1-5.3. The Fourier analysis of all four cases is then compared in section 5.4.

Applied distortion stagnation pressure and temperature patterns remain constant throughout the four simulations while the swirl was parametrically varied. Simulation contour solutions for static pressure are seen in Figures 21 through 24. The figures show flow from left to right and fan blade motion downward. Figures 21 and 22 are of the same pressure results but utilize two different scales for the flood plots, which highlight different aspects of the flow. Shock structure flow is highlighted using Figure 21 where upstream distortion convection is highlighted using Figure 24.

Solutions show varying blade-to-blade passage shock structure and bow wave propagation angle, specifically as the blades move past the counter-rotating vortices as seen in Figures 21 and 22. As case a = 0.0 exhibits zero swirl, the blade-to-blade pressure variation is much less obvious while the a = 1.5 case shows distinguished regions of high pressure post passage shock. As the blades approach the twin swirl section in the a = 1.5 case, denoted with blades 14 through 16, bow wave propagation distance is increased and passage shock strength remains relatively constant. However, once past the twin swirl, passage shock pressure magnitudes spike and reveal a much larger area of high pressure downstream of the shock.

In Figure 21 the a = 1.5 case with significant swirl, the passage shock spikes in magnitude every third blade when not passing the twin-vortex. This could be caused from the aerodynamic unsteadiness from the inlet distortion and should be further investigated. Also shown are the corresponding azimuthal planes for the pressure fields 0.007 inch downstream of the AIP. The zero-swirl case is nearly axisymmetric and features a high pressure bullseye caused by the potential field of the nose cone.

Furthermore, blades 14 and 18 characterize the bow propagation and shock structure differences stemming from the highly unsteady forcing function of the inlet distortion. Blade 14 approaches the swirl region, while 18 is just past the swirl region. Figures 21 and 22 show bow wave propagation angle variation with location with respect to the twin-swirl vortex in cases a = 0.0 and a = 1.5.

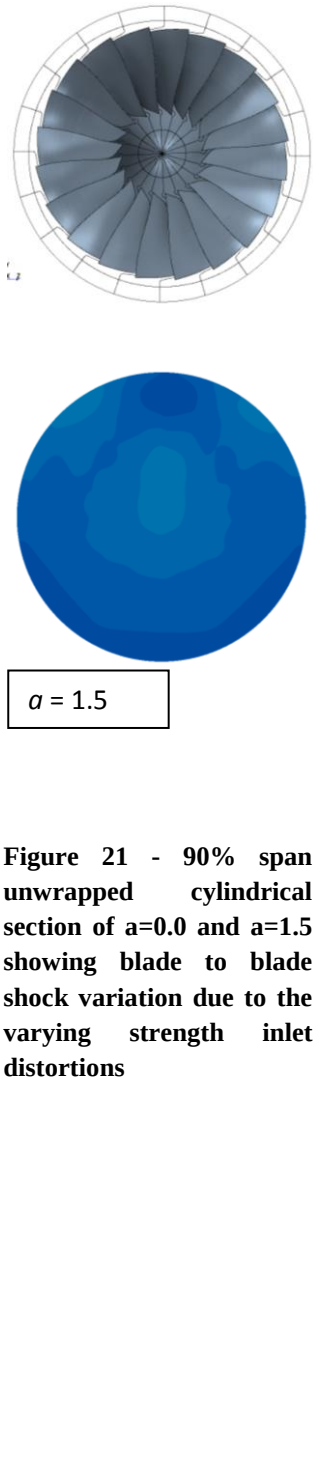

Figure 21 - 90% span unwrapped cylindrical section of a=0.0 and a=1.5 showing blade to blade shock variation due to the varying strength inlet distortions

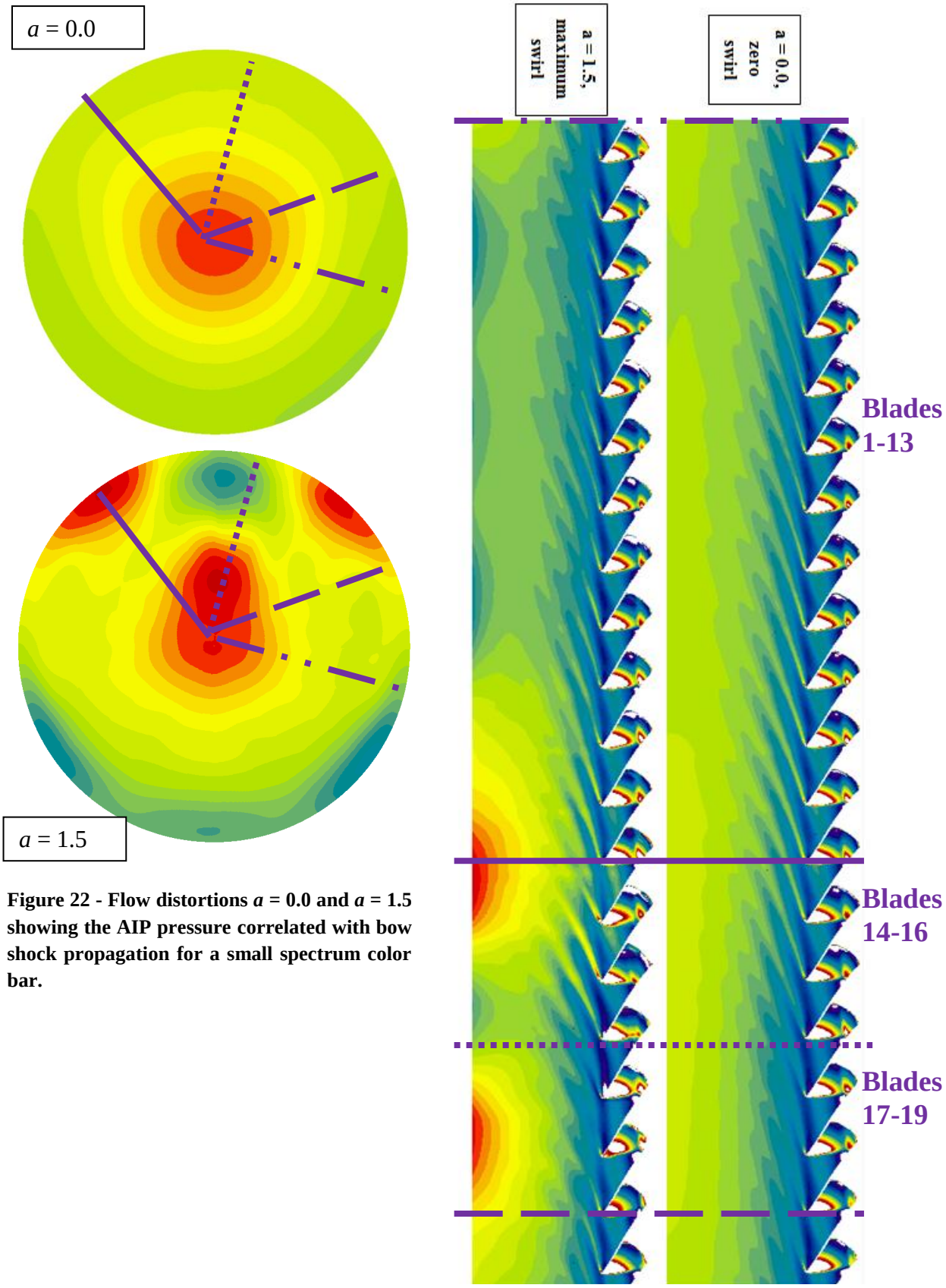

Figure 22 - Flow distortions *a* = 0.0 and *a* = 1.5 showing the AIP pressure correlated with bow shock propagation for a small spectrum color bar.

Figure 23 depicts blades 14 and 18 for case a = 0.0. As the unsteady forcing function of the a = 0.0 case is purely axial flow, the bow shock propagation changes from a point as the blades move past the swirl vortex to a point just past the swirl vortex. The change in bow wave propagation angle is subtle in case a = 0.0. However, the amount of swirl increases incrementally with increases in a. Figure 24 shows case a = 1.5 and indicates the effect of the unsteady swirl factor on the flow physics. The bow wave propagation angle changes significantly between blades 14 and 18 as shown in Figure 24. In addition, the shock structure in the a = 1.5 case has much more variation between blades 14 and 18 than the a = 0.0 case.

The bow wave integration with the passage flow is significant in both cases. For blade 18, bow waves caught between blades 18 and 19 reflect off of blade 19 and interact with the passage shock. On the blade approaching the swirl, bow wave reflection dies out before affecting the shock structure. It is due to the bow wave movement between blades 14 and 18 that the shocks on the surface of the blade are jumping locations as the blades pass the twin vortex swirl region.

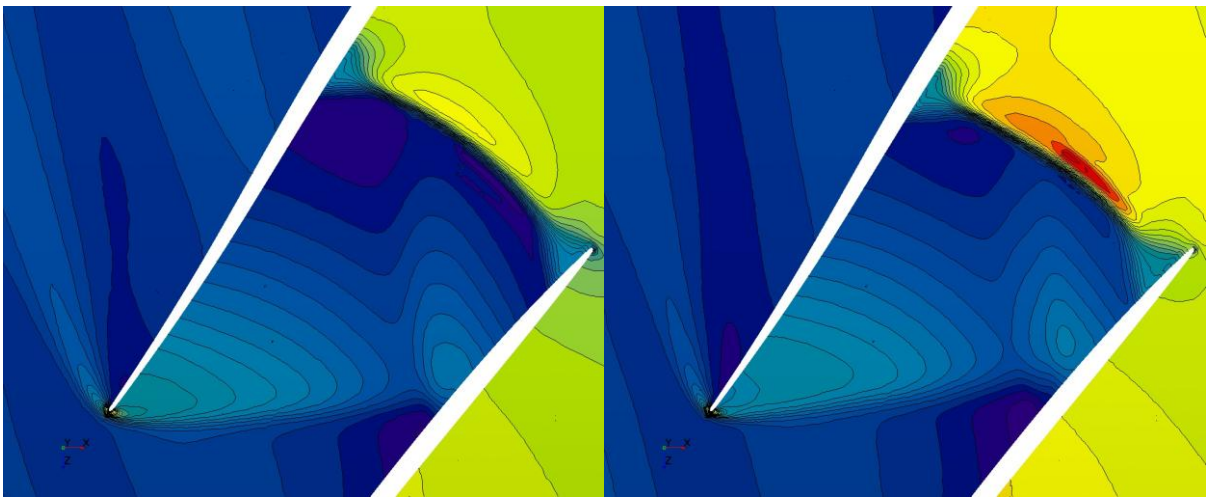

Figure 23 - Subtle changes in bow wave propagation angle for case a = 0.0. Blade 14 is shown on the left while blade 18 is shown on the right.

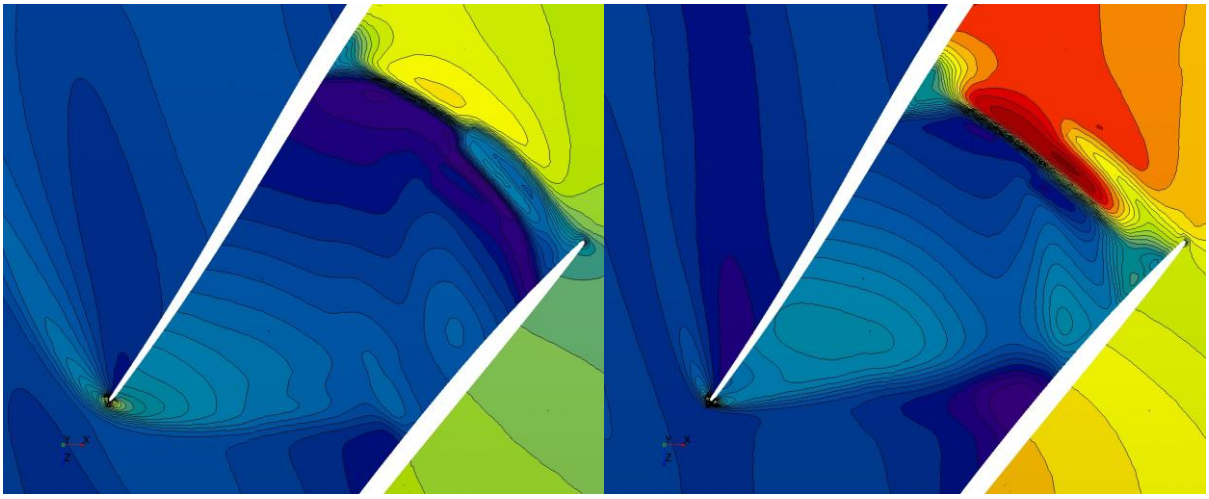

Figure 24 - Significant changes in bow wave propagation angle for case *a* = 1.5. Blade 14 is shown on the left while blade 18 is shown on the right.

5.2 Mid-passage Flow Structure Differences

As shown previously, shock motion is more prevalent in the a = 1.5 case as the upstream forcing function is composed of two counter-rotating vortices. The shock motion is investigated further utilizing a line probe traced midway between two blades. This method of investigation enables the difference between the two inlet distortions to be shown for not only the pressure but also the three-dimensional velocity field. Figure 25 shows plots of static pressure and the three directional velocity components on the line traced midway between blades 14 and 15 and blades 18 and 19 for cases a=0.0 and a=1.5. The green line represents the passage between blades 14 and 15. This is where the blades approach the swirl. The red plot represents the passage between blades 18 and 19. This is where the blades move past the swirl. Case a=0.0 static pressure shows minuscule change in shock location and bow propagation formation between the location approaching the swirl region and the location past the swirl vortex.

On the contrary, case *a*=1.5 static pressure shows differences in the way shock structure is established. Bow waves caught in between blades 18 and 19 get pushed towards the trailing edge and have a greater influence on the pressure jump. Note that the pressure between blades 14 and 15 is similar for both cases.

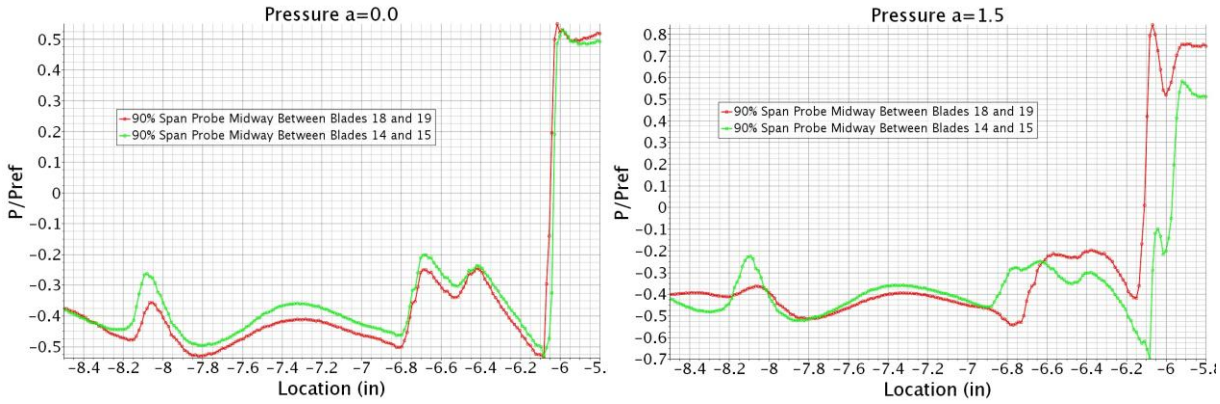

Figure 25 - Pressure along a line probe mid-span between blades 14 and 15 (green) and blades 18 and 19 (red).

5.3 Time Domain Blade Loading

Shock motion is apparent when comparing the static pressures on the different blade surfaces. Figure 26 shows the pressure and suction surfaces of blades 14 and 18 for the *a* = 0.0 simulation while Figure 27 shows the pressure and suction surfaces of blades 14 and 18 for the *a* = 1.5 simulation. The suction surface of all cases exhibits a region of low pressure towards the center of the blade (purple). This is due to bow wave propagation created from a neighboring blade as mentioned before. Such a low pressure region is manifested in different patterns that

have the potential to vibrate the blade at different frequencies and is shown in Figures 26 and 27.

For instance, the low pressure region on the suction surface of blade 14 for a = 0.0 and a = 1.5 takes the form of two stripes connected by a low pressure contour that does not extend to the leading edge of the blade. Conversely, the low pressure region on the suction surface of blade 18 for a = 0.0 and a = 1.5 has moved toward the leading edge. In addition, it contains only one

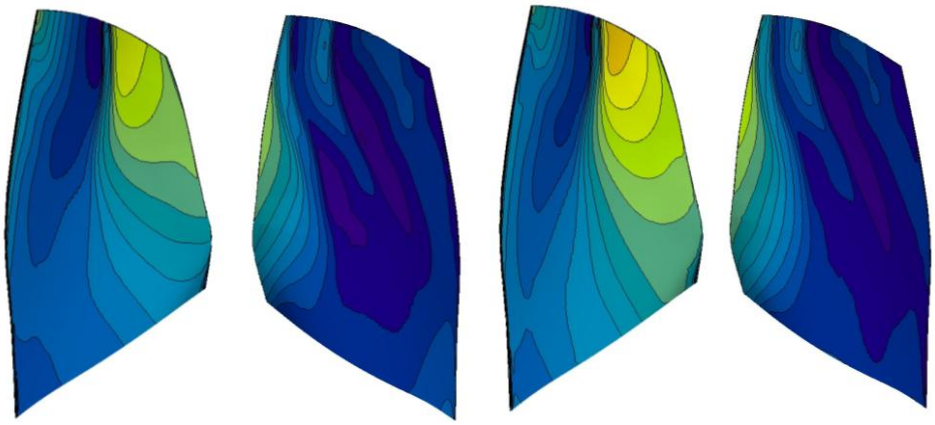

Figure 26 - a = 0.0 pressure and suction surface for blades 14 and 18.

stripe of extremely low pressure. These results show shock motion as the blades pass the swirl

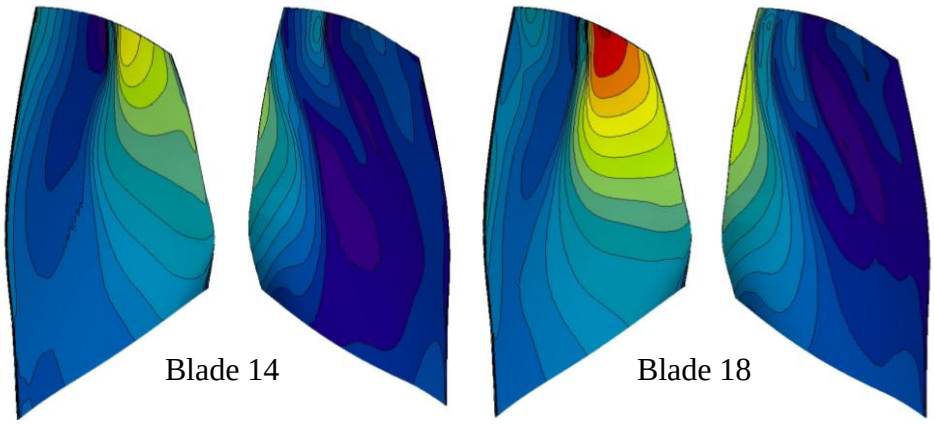

Figure 27- a = 1.5 pressure and suction surface for blades 14 and 18.

region.

5.4 Fourier Analysis

The development of the flow unsteadiness field is presented by tracking changes in the frequency spectrum along a streamline that begins at the AIP and terminates at one leading-edge diameter upstream of the stagnation point on the fan blade at 90% span location. Because of the quick changes observed near the blade and the large span of magnitude variation, the predictions are presented on log and semi-log plots. The abscissa represents distance *D* from the blade leading-edge stagnation point normalized by the rotor blade axial chord length *B*. From this perspective, flow moves from right to left. The AIP is at station 2.78, the nose cone tip at 1.40 and the blade leading edge is at 0.0.

5.4.1 Convected Streamline Decomposition

The time-mean, also referred to as harmonic 0, pressure and axial, tangential, and radial velocity values are shown in Figure 28. Pressure is shown to spike abruptly as the streamline approaches the blade leading edge, Figure 28a. Tracing the flow from the AIP in 28b indicates a global acceleration of the axial flow until it approaches the blade, crosses the detached bow shock and rapidly decelerates. Ripples are encountered at stations 0.6 and 1.1, caused by the bow wave propagation of the second and third neighboring blades. The flow has its strongest dependency on the swirl parameter at these locations. The time-mean tangential and radial velocity components are small (each approximately 2 percent of Q_{ref}) indicating negligible bulk swirl.

Tangential and radial velocities shown in Figure 28c and 28d reveal abrupt increase in rotational velocity upon entrance of the AIP for all parametric cases. This is due to the influence of the rotor. Similar results show bow wave propagation interacting with upstream distortion convection, causing ripples at the 0.6 and 1.1 locations. Furthermore, for all a cases, the solutions appear very similar with the exception of the tangential velocity where a small discrepancy

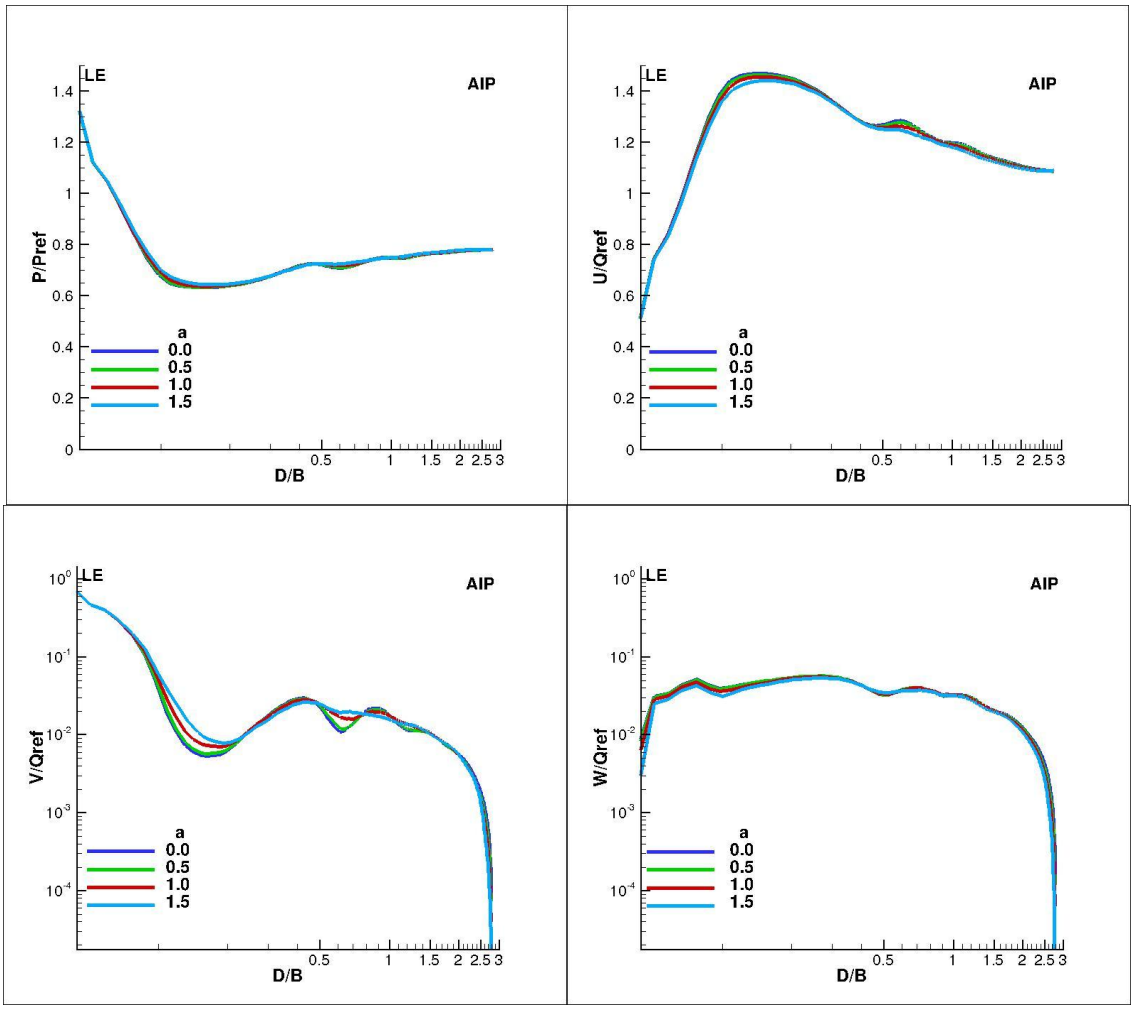

Figure 28 - Time-mean streamline traced from the AIP to rotor 4 leading edge.

occurs at the 0.25 and 0.75 locations.

Figure 29 summarizes the spectral magnitude results for the pressure, axial, radial, and tangential velocity components of the streamline at a point just downstream of the AIP. Figure

30 summarizes the peak spectral magnitude results for the pressure, axial, radial, and tangential velocity components near the blade stagnation point. It is in these plots that a comparison can be made between how convection of the inlet distortion affects the flow structure at rotor 4's leading edge.

The top rank sensitivities near the AIP surface are harmonics one, three, and six; while the lowest rank is harmonic two. In that sense, the AIP correlates with Figure 30 and the harmonics near rotor 4's leading edge. However, the first harmonic slopes are of opposite sign, leading to the belief that flow could be influenced by phasing. The curves are linear to quadratic, as well, and are monotonic, except for the two exceptions in the axial velocity (H2 and H4).

Each flow variable exhibits the trends that the first harmonic loses energy while the higher harmonics gain energy as swirl is increased. Plot magnitudes are not equivalent for Figures 29 and 30. For the pressure and velocity components, the first and second rank sensitivity to swirl parameter is seen in the sixth and third harmonics, the least sensitivity in the second harmonic. All curves are monotonic and exhibit linear to quadratic variation with the swirl parameter.

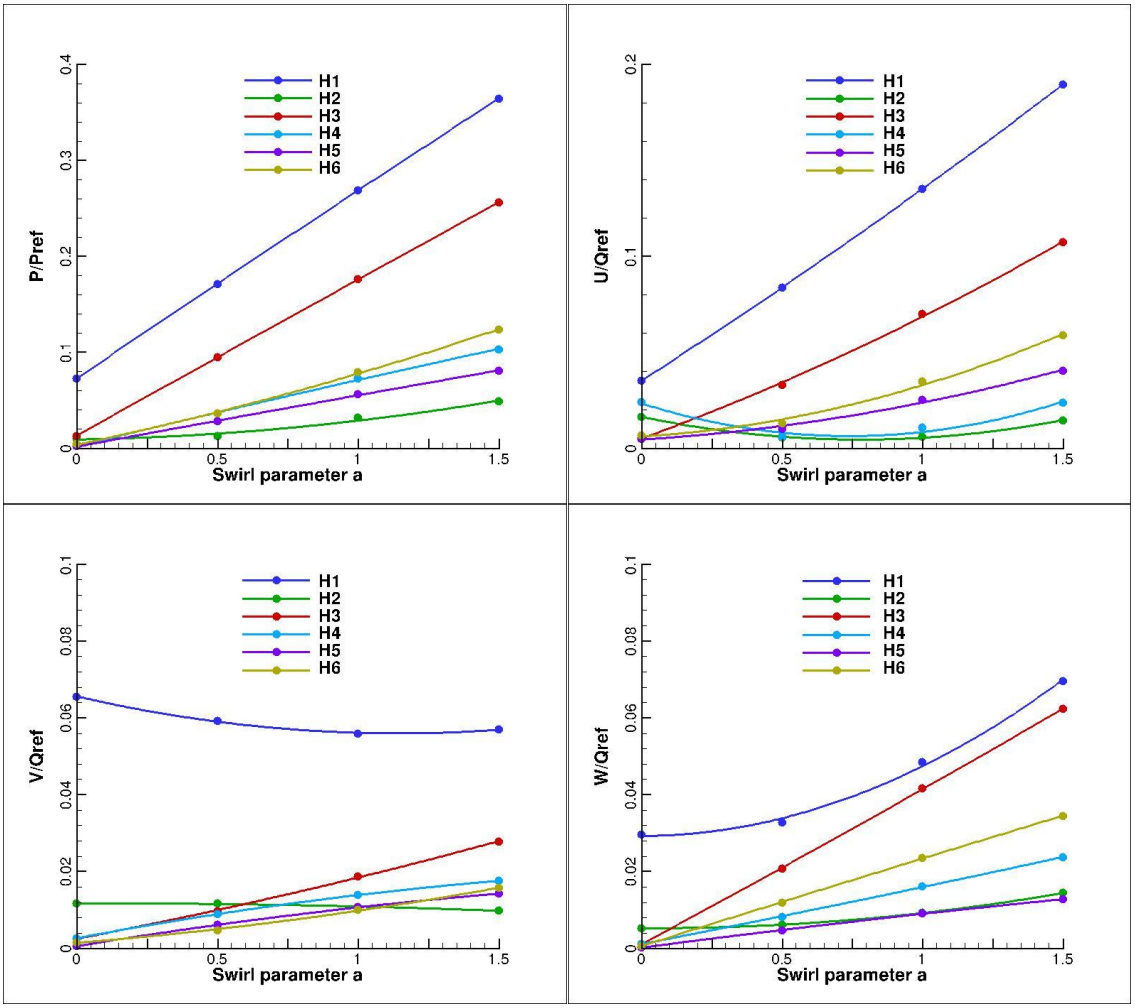

Figure 29 - Peak spectral magnitude of pressure, axial, tangential, and radial velocity components near the AIP surface.

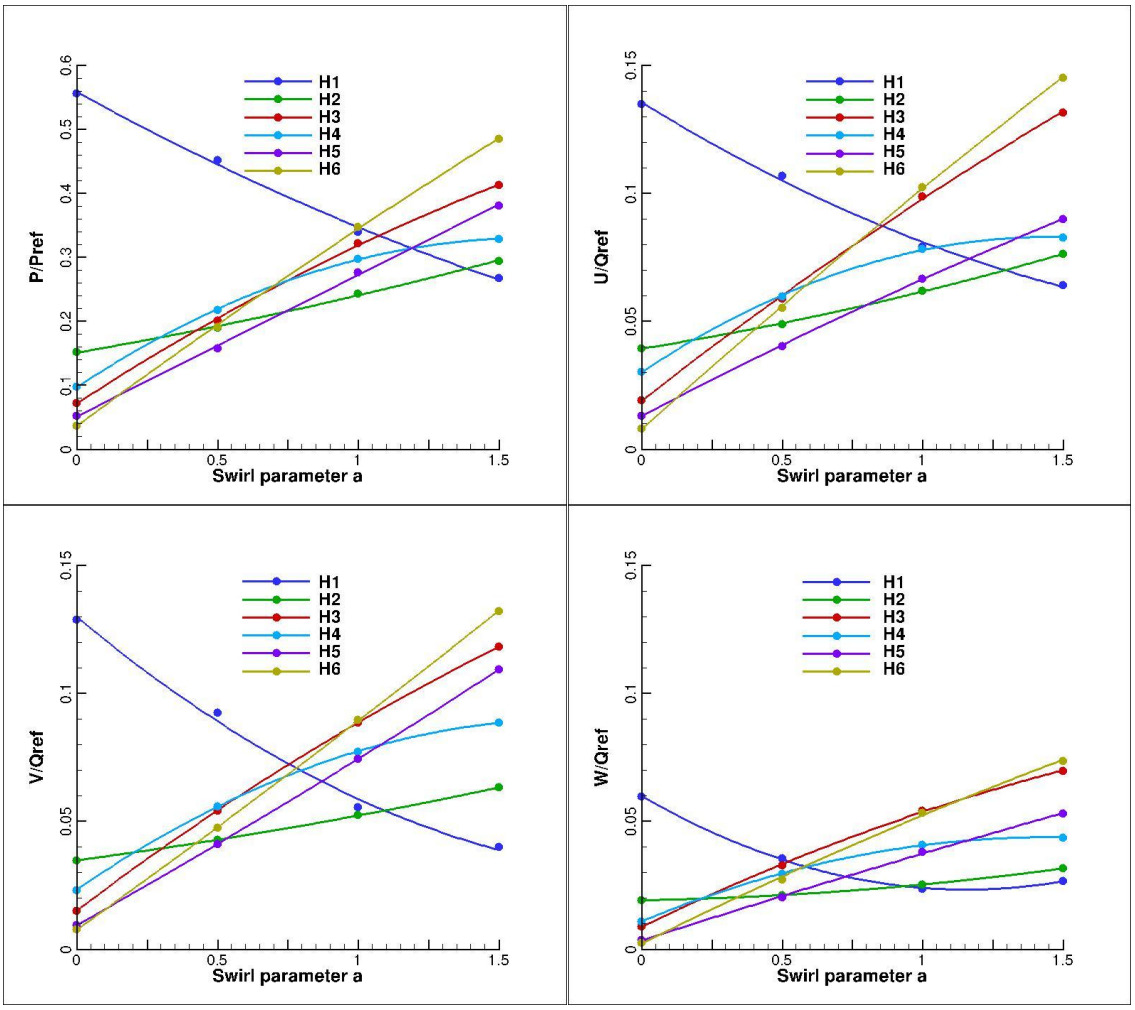

Figure 30 - Peak spectral magnitude of pressure, axial, tangential, and radial velocity components near the leading edge stagnation point.

The pressure frequency spectrum, seen in Figure 31, shows harmonics 1 through 6 in the quad chart for the four swirl cases. The pressures are sampled along the same streamline seen in Figure 28. In depth pressure variation is shown in harmonics 1 thorough 6. All harmonics show oscillation as the streamline is traced toward the rotor 4 stagnation point. The highly oscillatory pressure measurements are likely due to bow wave propagation from neighboring blades. The oscillation is shown to decrease with increasing swirl. Peak pressure occurs near the blade surface for lower swirl cases (most obviously in the a = 0.0 H1 sample). However, the peak

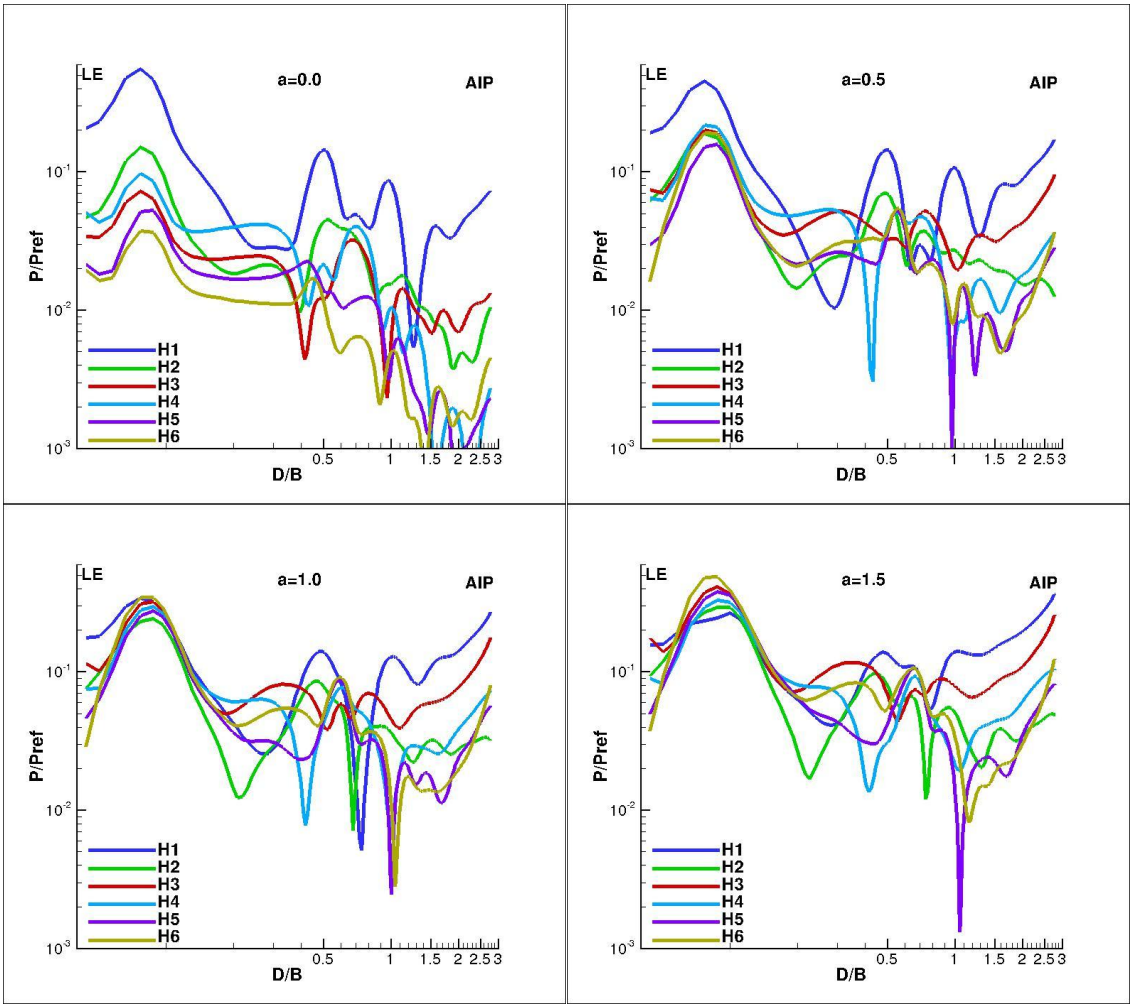

Figure 31 - Pressure frequency spectrum along streamline at 90 percent span.

pressure for the *a*=1.5 case is seen on the AIP surface. Minimum pressure is seen in the form of a large negative spike in H5 in all cases.

The axial velocity frequency spectrum is shown in Fig. 32. Harmonics 1 through 6 are presented as a quad chart representing the four magnitudes of swirl parameter. For all swirl parameter cases, the axial magnitudes initially decrease rapidly from the AIP with few exceptions. Magnitudes rise and fall upon encountering the series of bow shocks from the neighboring blades and the stagnation blade. The peaks have uniform alignment nearest the blade

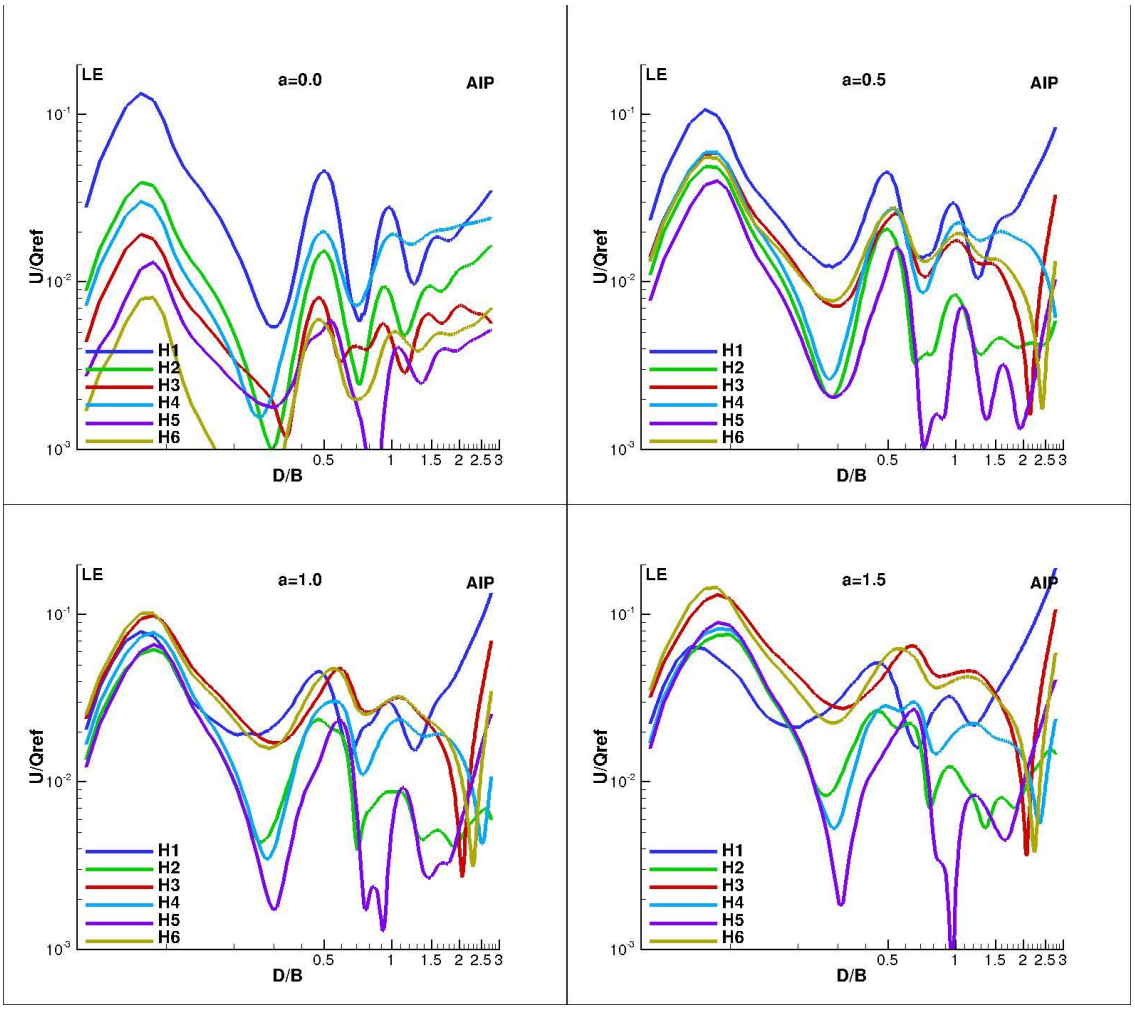

Figure 32 - Axial velocity frequency spectrum along streamline at 90 percent span.

for all swirl cases. However, less precise alignment is seen when the swirl increases and for shocks encountered farther from the blade. For the peaks nearest the blade, as the swirl is increased, the trend is for the first harmonic to loose strength and the higher harmonics to gain.

The tangential velocity frequency spectrum is shown in Fig. 33. For the zero-swirl case, not withstanding, a tangential velocity is induced, and mainly in the first and second harmonics. For the non-zero swirl cases, tangential velocity is increased for all harmonics. The magnitude shifts are not as volatile when the bow shocks are encountered, as compared to the axial velocity spectrum, even though their peak magnitudes are of the same order. This is attributed to the large majority of flow and kinetic energy being in the axial direction and only small amounts being

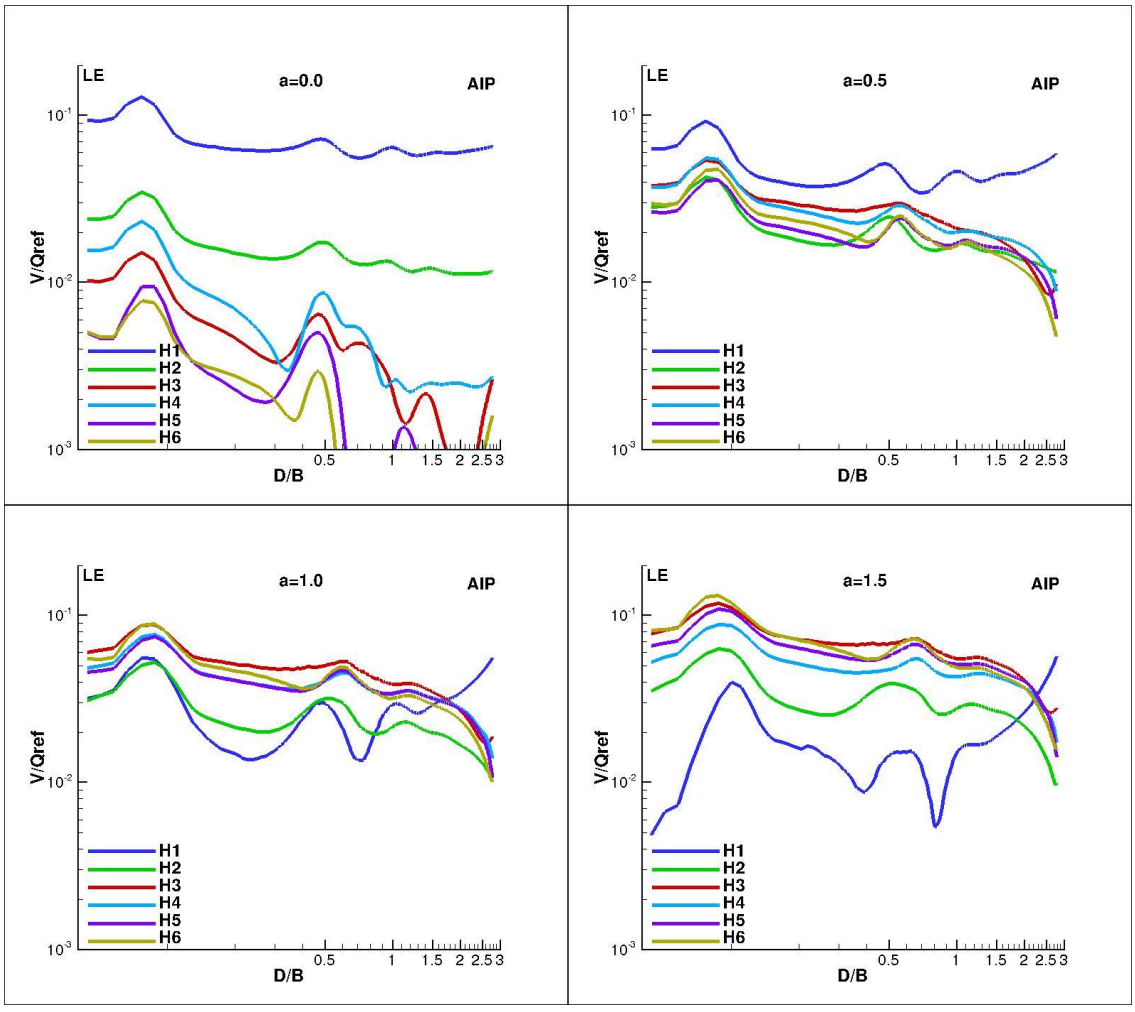

Figure 33 - Tangential velocity frequency spectrum along streamline at 90 percent span.

radial and tangential.

The radial velocity frequency spectrum is shown in Fig. 34. The spectrum shows small amounts of variation for cases a = 0.5, a = 1.0, and a = 1.5. The greatest variation in harmonic magnitude is in harmonic 1 for the three higher swirl cases. It is shown in case a = 1.5, the magnitude greatly drops off after the AIP and tends to oscillate more than the higher harmonics. Similarly, harmonics 3 through 6 have small magnitudes in the zero swirl case.

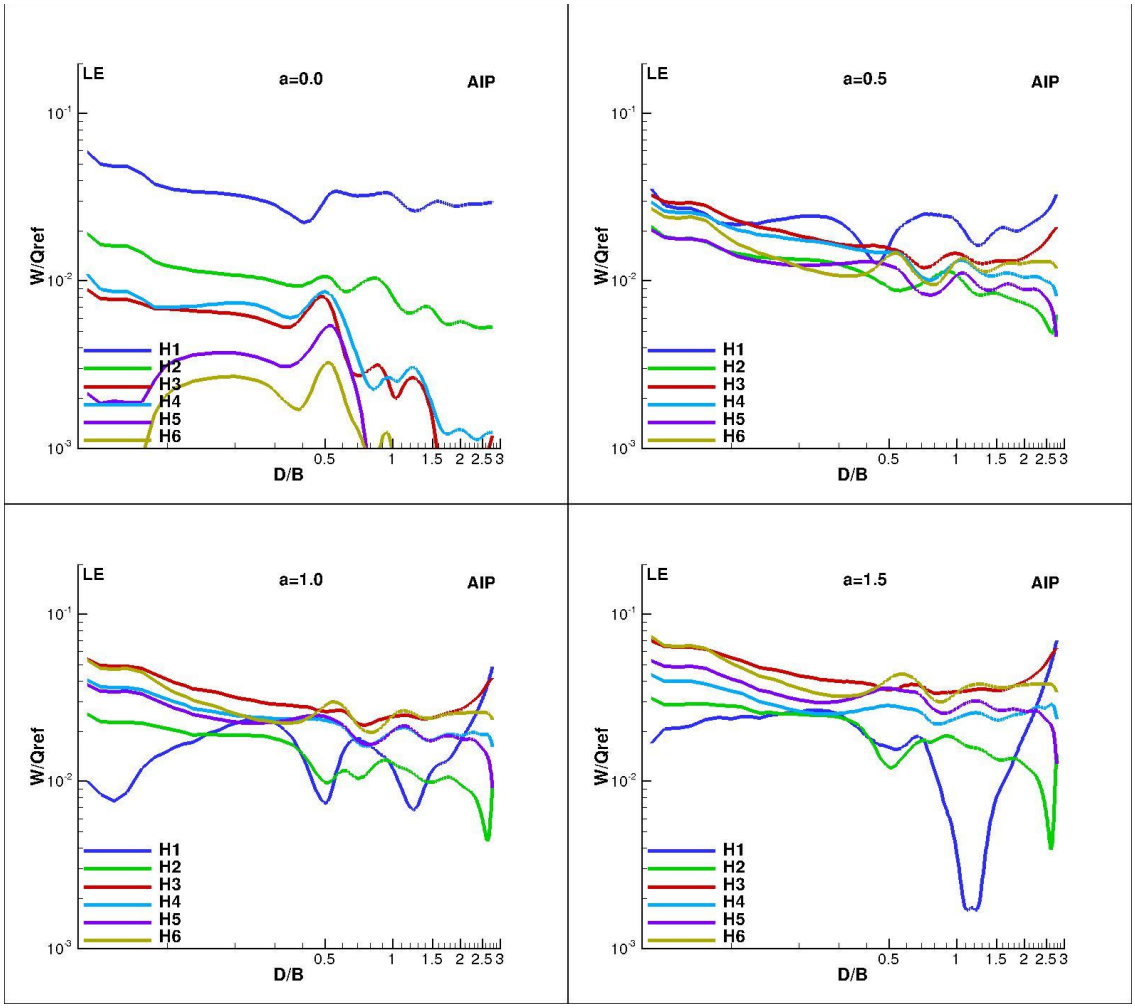

Figure 34 - Radial velocity frequency spectrum along streamline at 90 percent span.

The trend for all cases shows a substantial decrease in the energy of H1 with increase of swirl. For axial, radial, and tangential directions, H1 starts with significantly higher energy

content than H2-H6 for a = 0.0. By the a = 1.5 case, H1 plummets to the lowest energy out of all harmonics.

5.4.2 Modal Blade Loading

Blade loading subject to the inlet distortion was investigated. H1-H6 surfaces pressures for the pressure, suction, and tip surfaces were sampled at each surface mesh cell center and multiplied by the associated surface mesh element area. The subsequent element forces were integrated to produce a single representative force for each of the 6 harmonics in 3 dimensions. Figure 35 shows harmonic blade loading versus the amount of swirl applied to the inlet. Figure 35a is the magnitude of loading while 35b, 35c, and 35d are x, y, and z components, respectively. The x component corresponds with axial flow, while the y and z components are analogous to the tangential and radial components.

For all directions, excluding tangential, the force increases with increasing swirl for all harmonics. Similarly, the number of harmonic related directly to the magnitude of blade loading. However, the tangential forces did not follow the common trend. Harmonics 3 and 4 exhibited a negative slope, while 2, 5, and 6 exhibited positive slope. This is seen in Figure 35c. Note: the magnitude of tangential and radial load are an entire magnitude smaller than axial loading and therefore may be insignificant to modal response.

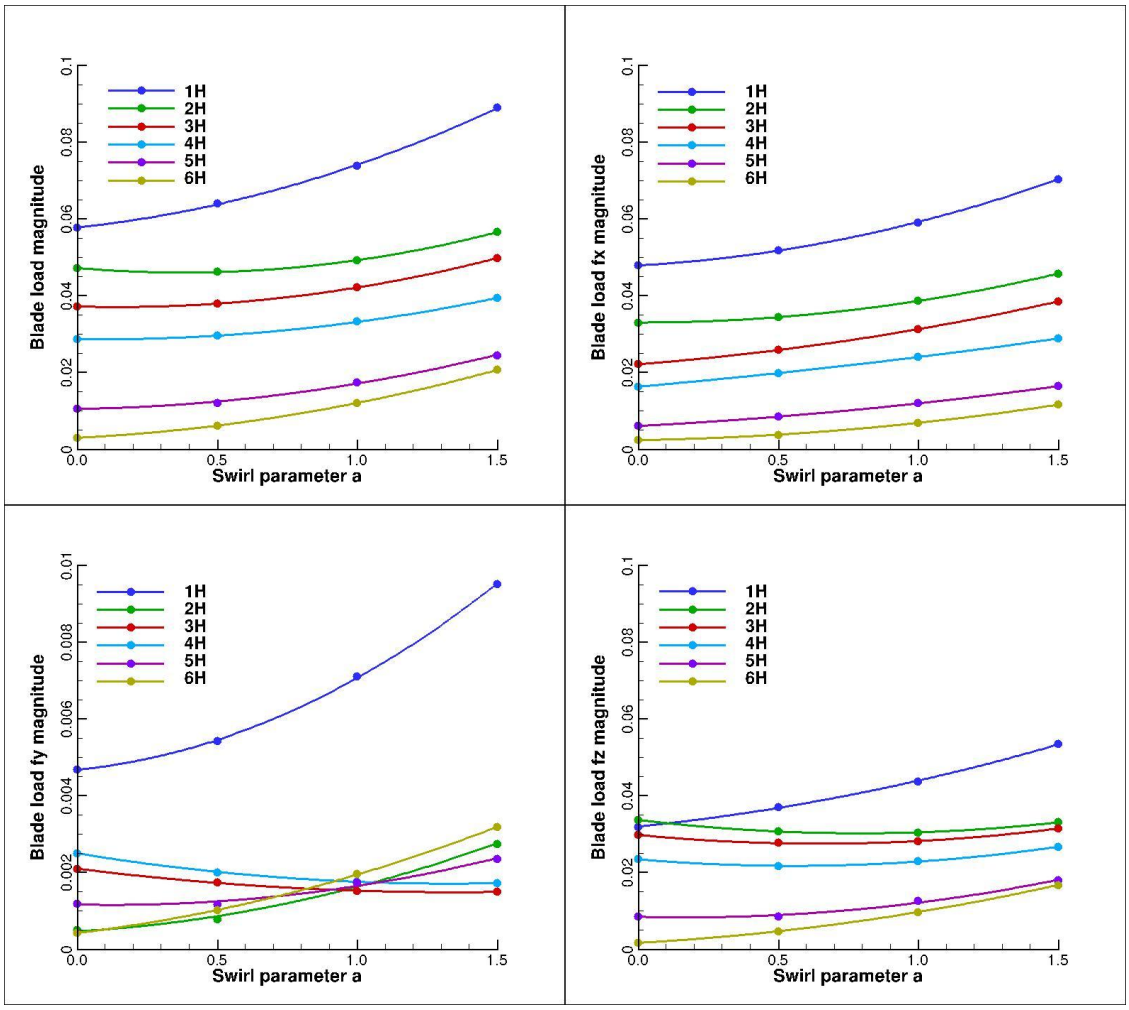

Figure 35 - Harmonic blade loading influenced by swirl.

Modal forces were calculated for the three lowest blade vibration modes. Figure 15 presents a Campbell diagram for the fan which indicates the mode/harmonic pairs of interest: 1B/2E, 2B/5E, and 1T/6E. However, to broaden the population of calculations in order to discover trends, for each blade vibrational mode, a dot product was formed with each of the six harmonics of pressure, consequently producing several modal forces that are hypothetical for this rotor design.

The modal force F is calculated by the surface integration of the product of vibrational mode shape vector, surface normal vector, surface pressure, and elemental area over the blade region,

$$F = \oiint_S \vec{\varphi} \cdot \vec{n} \; p \, dA \tag{29}$$

The modal force represents the strength of the forcing function acting on the vibrating blade. The larger the modal force, the larger the vibrational displacement and stress in the blade. As seen in Section 4.6, the vibratory mode shapes for 1B/2E, 2B/5E, and 1T/6E correspond to crossings of vibration frequency and engine order excitation on the Campbell diagram.

Figure 36 presents the three resulting families of modal forces. The modal forces are monotonic with swirl, with two exceptions: 1B/H1 and 2B/H1. Similarly to the blade loading in Figure 36, modal forces gradually increase with swirl parameter, with the exception in 2B/H1 that has a large magnitude for a = 0.0 and a = 1.5, but dips down for a = 0.5 and a = 1.0. The curves are linear to quadratic and concave upward, with the exception 2B/H4, which is concave downward.

Maximum modal forces show that 1B sees the most energy while 1T contains approximately half the 1B energy. 2B sees approximately one third the 1B energy. Results show that the 2B could be excited in patterns that are not obvious as a gradual increasing modal force with increasing swirl.

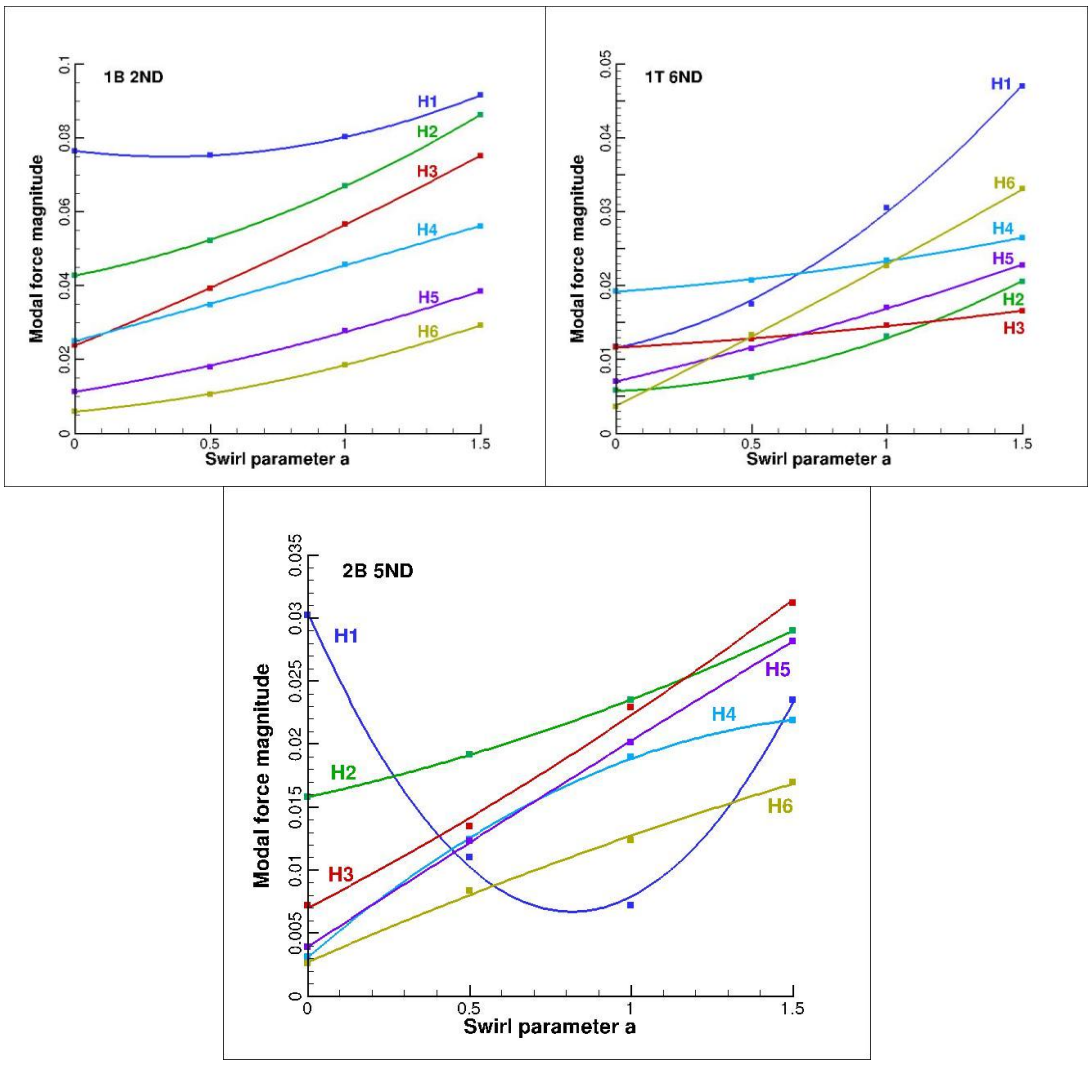

Figure 36 - Modal forces influenced by swirl.

5.4.3 Harmonic Blade Loading

Blade surface pressures for harmonics 1 through 6 are shown in Figures 37 through 42 while the integrated force quantities and their percent change with swirl parameter are shown in Tables 5 and 6. The effects of the shocks are manifested at the mid-chord pressure surface (PS)

Table 6. Forces Integrated Over Blade Surface (lbf)

Harmonic:	0	1	2	3	4	5	6
a = 0.0	96.17	4.73	4.24	2.81	1.97	0.70	0.19
a = 0.5	95.98	5.28	3.96	2.76	2.01	0.79	0.37
a = 1.0	94.74	6.33	4.08	3.00	2.24	1.09	0.70
a = 1.5	93.62	7.75	4.59	3.52	2.62	1.53	1.19

Table 7. Percent Change in Harmonic Force

Harmonic:	0	1	2	3	4	5	6
a = 0.0	0.00%	0.00%	0.00%	0.00%	0.00%	0.00%	0.00%
a = 0.5	-0.20%	11.05%	-6.85%	-1.72%	2.11%	12.18%	62.28%
a = 1.0	-1.49%	28.87%	-3.87%	6.47%	12.58%	44.22%	113.40%
a = 1.5	-2.69%	48.38%	7.87%	22.35%	28.17%	74.44%	143.85%

and trailing edged suction surface (SS). As the swirl increases, high pressure is seen to penetrate inboard toward the hub, while the regions at the tip broaden. The broadened region indicates larger shock motion sweep along the blade surface.

The rank of highest harmonic magnitude go in the order H1, H2, H3, H6, H4, H5. This implies that the greatest modal response will come from harmonics H1, H2, and H3. These harmonics all show the most significant harmonic energy near the trailing edge of the SS and near the center of the blade of the PS, both near the tip. Pressure on the surfaces show small variation near the blade hub.

Comparing the swirl cases for the highest and lowest harmonics, H1, H2, H5, and H6, it is shown that pressure contours do not change in pattern with increasing swirl, however change significantly in magnitude. This is not the case in H3 and H4, the pressure contour pattern not only changes in magnitude, it essentially inverts the location of higher pressure with increasing swirl. In the a = 0.0 (zero swirl case), the significant pressure is located near the hub, while in the a = 1.5 case the significant pressure is located near the tip.

A similar plot for the sixth harmonic is shown in Fig. 42. Compared to the second harmonic, although the peak magnitude has changed only 10 percent, the greater sensitivity to swirl is evident in the stark contrast between the patterns of least and greatest swirl. Further, there is stronger activity at the hub and concentrated closer to the tip and not penetrating

substantially below the 90% span mark. Magnitudes maximums range from 0.22 in the smallest harmonic to 0.90 in the highest harmonic leading to the belief that all harmonics can be

significant to blade mode shapes.

Integrated blade force quantities reveal blade loading differences with change in swirl magnitude. Such results are shown in Tables 6 and 7. The values show a decrease in blade force for harmonic 0 with increased swirl. However, as harmonic values increase, a trend of increased percent difference is seen. Harmonics 2 and 3 show an initial decrease in blade loading which subsequently grows by the a = 1.5 case. Phasing in the solution could lead to behavior such as this. In addition, the results show larger percent differences in the higher harmonics. For instance, a percent difference of 143.85 is shown between the a = 0.0 and a = 1.5 cases for harmonic 6.

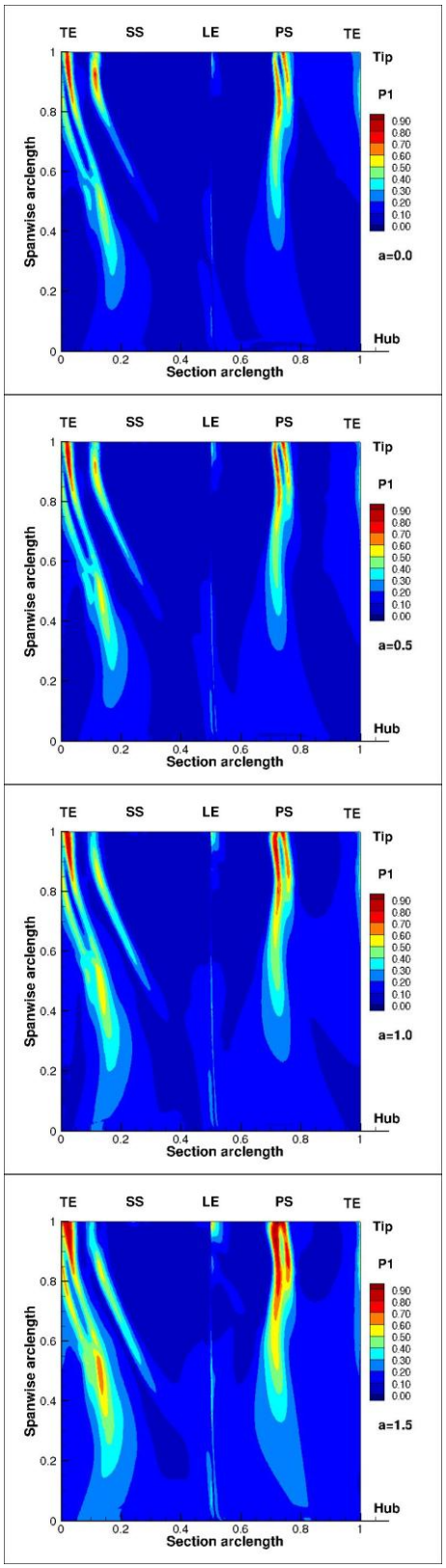

Figure 37 - Blade surface pressure harmonic 1.

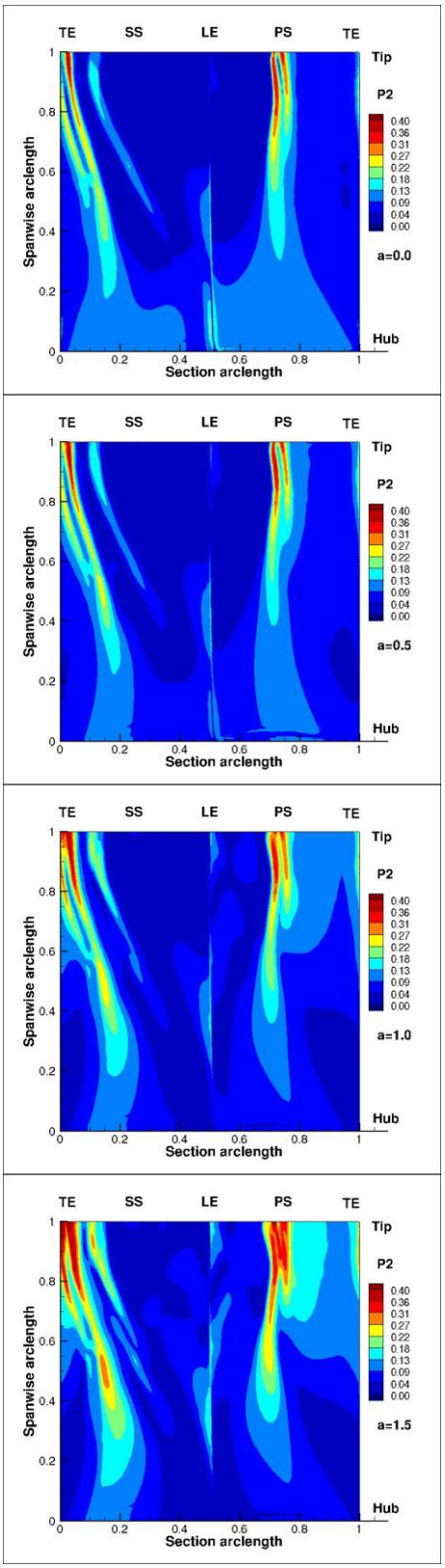

Figure 38- Blade surface pressure harmonic 2.

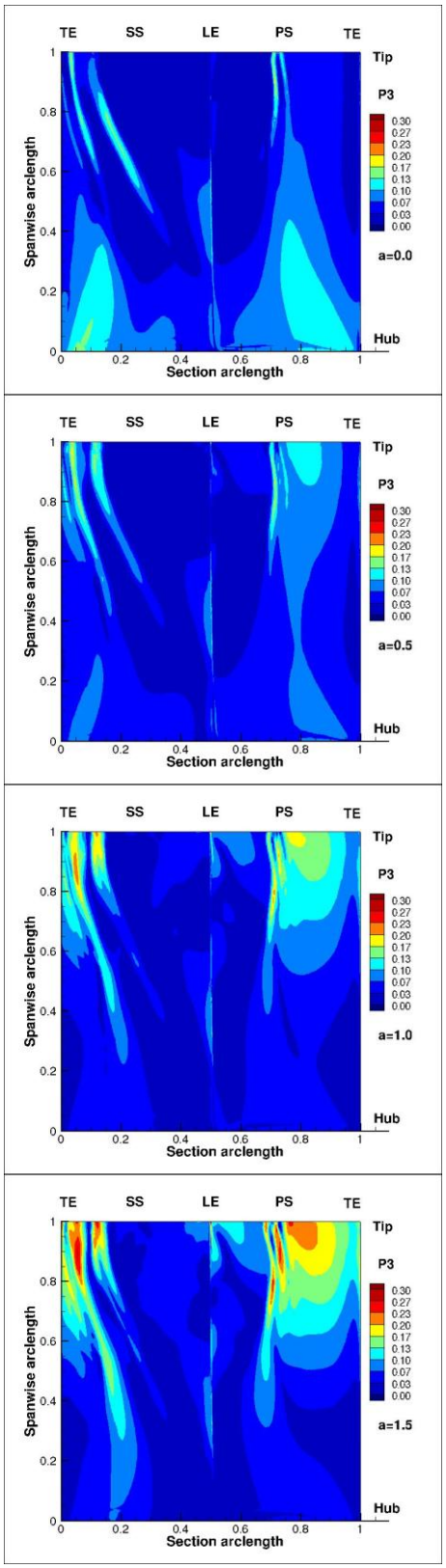

Figure 39- Blade surface pressure harmonic 3.

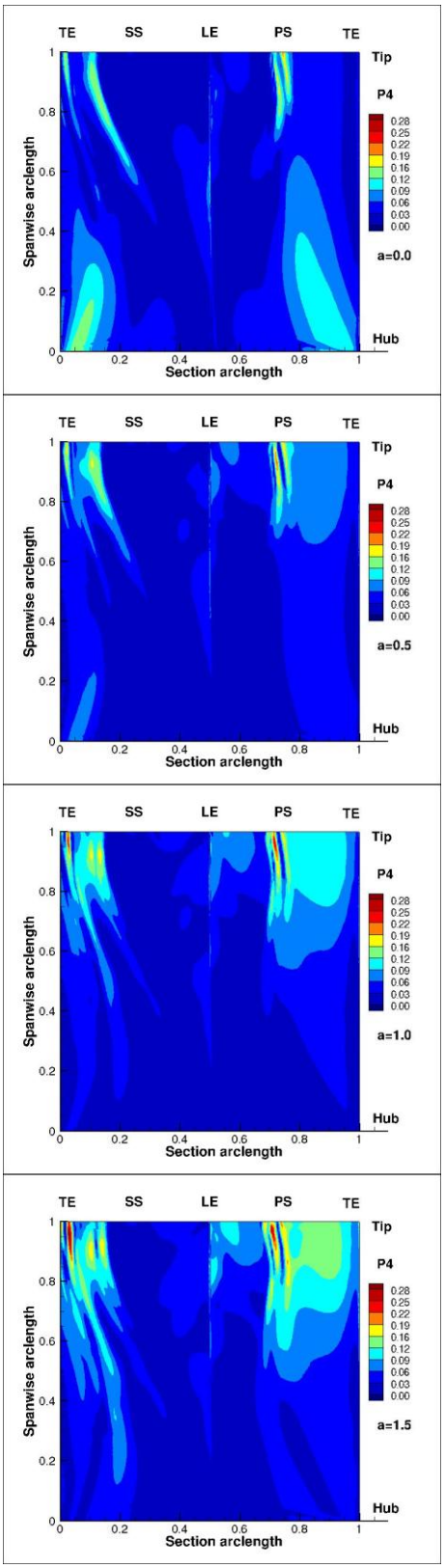

Figure 40- Blade surface pressure harmonic 4.

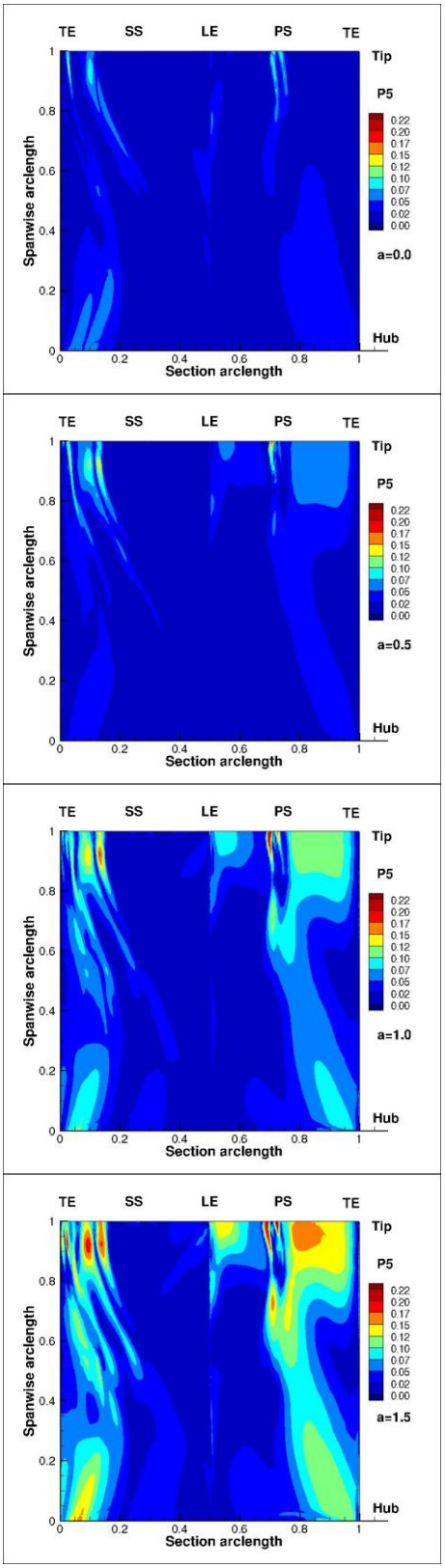

Figure 41 - Blade surface pressure harmonic 5.

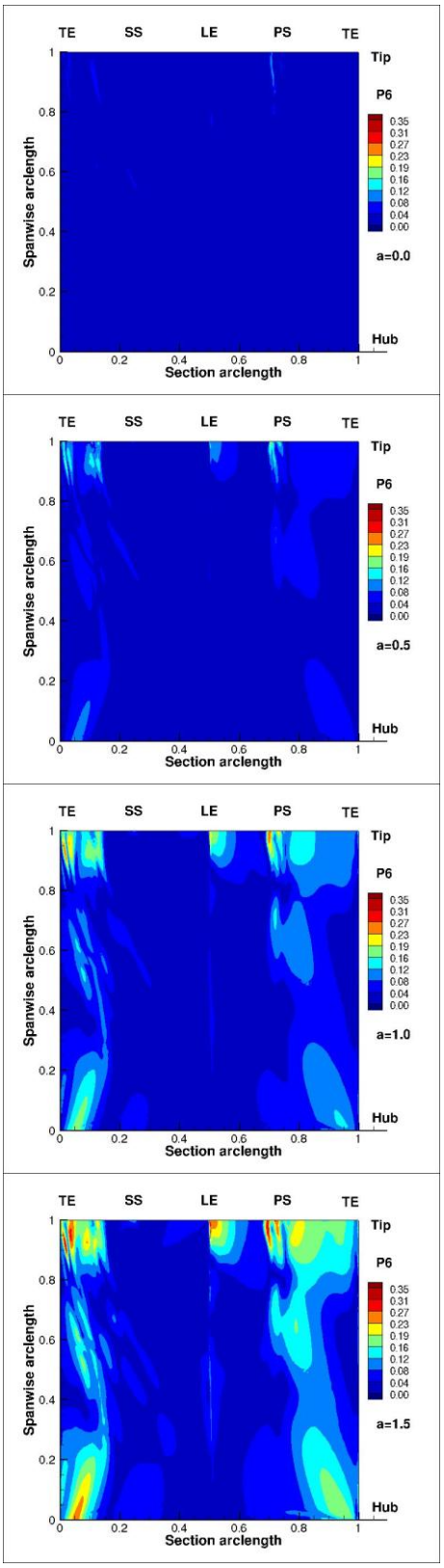

Figure 42- Blade surface pressure harmonic 6.

5.4.4 Shock Motion

The pressure spectrum along the mid-passage streamline at 90% span, Figure 43, indicates that the shock envelope of motion is 7 percent chord for the zero-swirl case and 12 percent chord for the high swirl case. This broadening along the chord manifests in all six harmonics. Such broadening flow structure is seen in Figure 44. Shock is defined as the location at which the propagation waves move faster than the speed of sound in the fluid causing discontinuous changes in the flow parameters. As flow accelerates over the airfoil, the flow compresses and results in sudden pressure, density and temperature rise. The combination of shock structure and motion of the shock cause blade loading which changes rapidly along the chord.

A 12 percent change in location towards the tip of the rotor could lead to highly unsteady moment arms and in turn cause extreme blade excitation. Improving the blade performance to account for a 7-12 percent chord shock motion is possible.

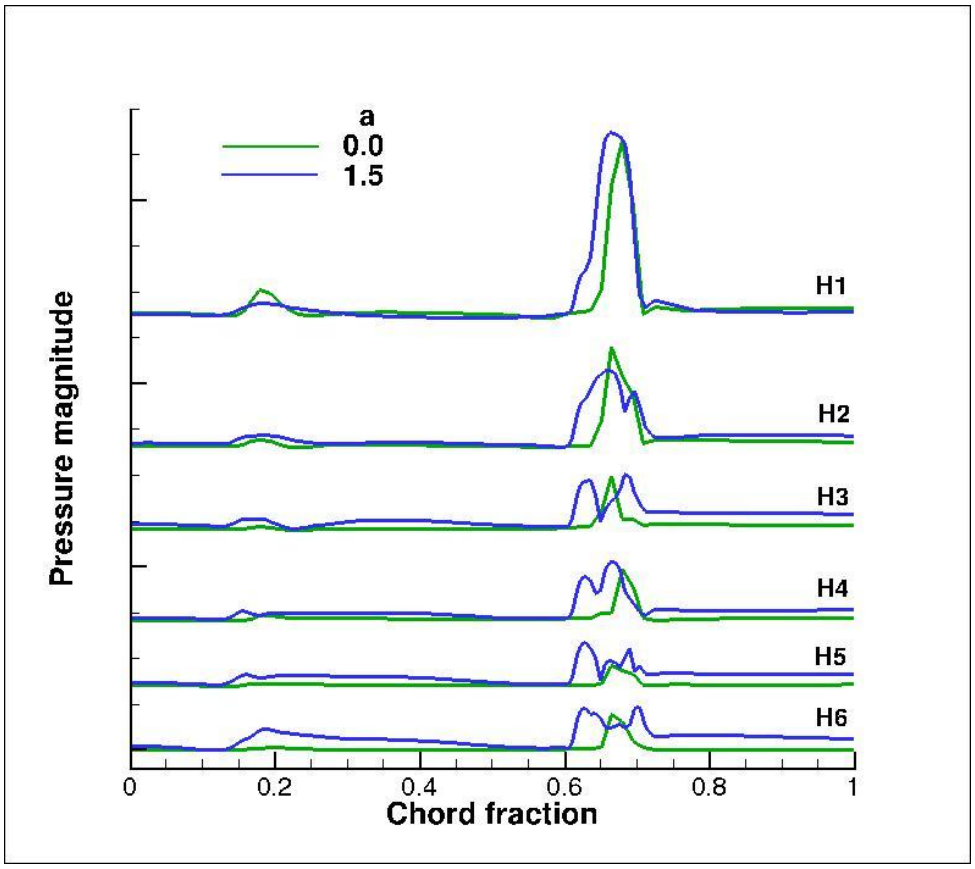

Figure 43 - Harmonics depicting shock structure movement in a mid-passage streamline.

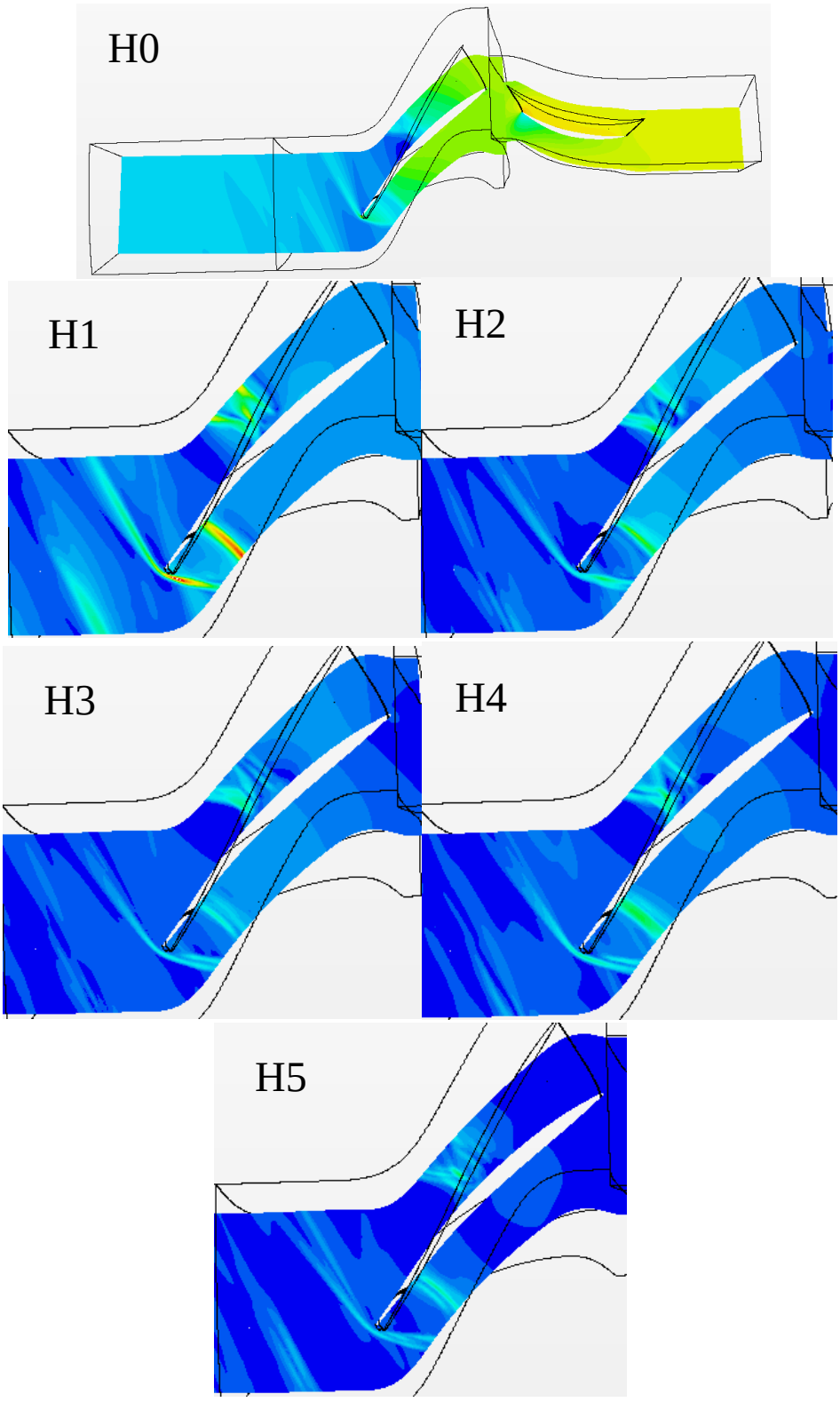

Figure 44 - Harmonic shock motion pressure contour plots.

6. CONCLUSION

6.1 Summary

A computational study was conducted to understand the influence of aircraft inlet flow distortion on the aerodynamic loading of a gas turbine fan stage. A single stage, transonic fan design with no inlet guide vanes was modeled with a commercial, computational fluid dynamics solver using a harmonic balance technique.

The inlet flow pattern, consistent with that of a homeomorphic variant of the M2129 duct, exhibited stagnation pressure distortion and a twin-swirl velocity distribution. The fan aeromechanical responses were investigated in a parametric study based on variations in the strength of the swirl velocity. In particular, a series of four CFD calculations were obtained for a range of swirl strength from 0.0 to 1.5. The effect of inlet flow distortion on the unsteady aerodynamic parameters of the fan blade was studied.

The aeromechanics investigation centered on the 90% span location, although computational data was obtained for the complete blade. Significant flow non-uniformity was found to be concentrated in the swirl regions with trends proportional to the swirl parameter. More specifically, the blades passing the location of twin-swirl exhibited higher pressure jumps than all other locations in the annulus. In addition, high harmonic content through a streamline propagating mid-passage revealed significant shock movement within a blade passage. Finally, a Fourier spectral analysis investigated unsteady inlet distortion convection to reveal the effect of swirl magnitude on blade loading.

6.2 Contributions

Results show modal force increases with the intensity of twin swirl, as shown in Figure 37. Modal forces were calculated for 1B, 2B, and 1T blade vibration modes and are monotonic with swirl, with two exceptions: 1B/H1 and 2B/H1. The curves are linear to quadratic and concave upward, with two exceptions, 2B/H4 and 2B/H5, which are concave downward. Harmonics 3 and 4 exhibited a negative slope, while 2, 5, and 6 exhibited positive slope for the tangential harmonic loading. This is assumed to be due to phasing in the solution.

The results of the parametric study show that even with a zero swirl parameter, non-zero swirl velocity components are induced just downstream of the AIP. This occurs as a result of the in-plane pressure gradients being preserved at the inlet boundary. If we simplify the analysis to two dimensions and take (*x*, *y*) and (*u*, *v*) to represent the (axial, tangential) directions and velocities, we begin with the Euler equation for the tangential direction.

$$\frac{-1}{\rho}\frac{\partial p}{\partial y} = u\frac{\partial v}{\partial x} + v\frac{\partial v}{\partial y}$$

Integrating in the axial direction from the AIP (station 0) to a small axial distance away (station 1), yields an expression for the induced tangential velocity,

$$v_1 = v_0 + \left(\frac{-1}{\rho u}\frac{\partial p}{\partial y}\right)_0 \Delta x + \left(\frac{-v}{u}\frac{\partial v}{\partial y}\right)_0 \Delta x$$

When $a = 0.0$, the first and third terms are zero, leaving only the in-plane pressure gradient to induce the tangential velocity.

When $a > 0.0$, all three terms induce the tangential velocity: the AIP velocity and the in-plane gradients of pressure and of tangential velocity. Referring back to the Euler equation, we see that once the tangential velocity is induced, the pressure field will not remain constant at its AIP distribution, but will also change with axial direction. Results show that the introduction of

swirl serves to transfer energy from the largest length scale (first harmonic) to smaller length scales (higher harmonics).

Finally, results showed that high levels of twin swirl intensity cause significant shock motion in the rotor passages and blade-to-blade flow variability for a given time snapshot. The passage response is sensitive to the proximity and direction of the twin swirl distortion.

6.3 Modeling Implications

With regard to modeling, the lessons learned of this research are

- When modeling a region upstream of the spinner cone, a structured mesh should be implemented to spatially resolve spinning modes near the centerline.
- Second-order accurate HB simulations diverge when the inlet distortion is applied. This is thought to be related to the large stock motion observed in the first-order accurate simulations.

6.4 Future Work

Further work is suggested to converge the inlet distortion HB solutions using the second-order accurate option, as the simulations of this study achieved convergence only for the first-order accurate option. Such a study would control mesh density, spinning mode density, and inlet distortion strength to understand requirements for second-order convergence.

REFERENCES

Arntz, Aurélien, Olivier Atinault, and Alain Merlen. "Exergy-Based Formulation for Aircraft Aeropropulsive Performance Assessment: Theoretical Development." AIAA Journal 53.6 (2015): 627-639.

Bakhle, Milind, T.S.R. Reddy, Gregory Herrick, Aamir Shabbir, and Razvan Florea. "Aeromechanics Analysis of a Boundary Layer Ingesting Fan." 48th AIAA/ASME/SAE/ASEE Joint Propulsion Conference & Exhibit (2012)

Bakhle, Milind A., T. S. Reddy, and Rula M. Coroneos. "Forced Response Analysis of a Fan with Boundary Layer Inlet Distortion." 50th AIAA/ASME/SAE/ASEE Joint Propulsion Conference (2014)

Besem, Fanny M., Robert E. Kielb, and Nicole L. Key. "Forced Response Sensitivity of a Mistuned Rotor from an Embedded Compressor Stage." Volume 7B: Structures and Dynamics (2015).

Burkardt, John, Qiang Du, Max Gunzburger, and Hyung-Chun Lee, "Reduced Order Modeling of Complex Systems." NA03 Dundee Biennial Conference on Numerical Analysis. 2003. pp. 29-38.

CD-Adapco, STAR-CCM+ User Guide, Version 10, "Harmonic Balance Formulation." 2015. Web.

Custer, Chad H. *A Nonlinear Harmonic Balance Solver for an Implicit CFD Code: OVERFLOW 2* Ph.D. Dissertation, Duke University, 2009.

Custer, Chad, Jonathan M. Weiss, Venkatarmanan Subramanian, Willian S. Clark, Kenneth C. Hall, "Unsteady Simulation of a 1.5 Stage Turbine Using an Implicitly Coupled Nonlinear Harmonic Balance Method," ASME Turbo Expo 2012. 2012.

Danforth, C. E., "Distortion Induced Vibration in Fan and Compressor Blades," 12th Aerospace Sciences Meeting, 1974.

Deck, Sebastien, Philippe Duveau, D'Espiney Paulo, and Philippe Guillen. "Development and Application of Spalart–Allmaras One Equation." *Aerospace Science and Technology* 6 (2002): 171-83. 11 Jan. 2002.

Ekici, Kivanc, Hall, Kenneth C., "Nonlinear Analysis of Unsteady Flows in Multistage Turbomachines Using Harmonic Balance," AIAA Journal 45:5, (2007): 1047-1057.

Ferrar, Anthony, and O'Brien, Walter. "Flow in Boundary Layer Ingesting Serpentine Inlets." 47th AIAA/ASME/SAE/ASEE Joint Propulsion Conference & Exhibit (2011)

Hall, K. C., J. P. Thomas, and W. S. Clark. "Computation of Unsteady Nonlinear Flows in Cascades Using a Harmonic Balance Technique." AIAA Journal 40 (2002): 879-86.

Hall, Kenneth C., Thomas, Jeffrey P., and Clark, W. S., "Computation of Unsteady Nonlinear Flows in Cascades Using a Harmonic Balance Technique," AIAA Journal 40:5, 2002, pp. 879-886.

Hamed, A., and Numbers, K., "Inlet Distortion Considerations for High Cycle Fatigue in Gas Turbine Engine", 33rd Joint Propulsion Conference and Exhibit, AIAA Paper No. 97-36488, 1997.

Hardin, Larry, Gregory Tillman, Om Sharma, Jeffrey Berton, and David Arend. "Aircraft System Study of Boundary Layer Ingesting Propulsion." 48th AIAA/ASME/SAE/ASEE Joint Propulsion Conference & Exhibit (2012)

He, L., “Fourier Methods for Turbomachinery Applications.” Progress in Aerospace Sciences 46. (2010) 329-341.

Kays, W. M., Crawford, M. E., and Weigand, Bernhand. Convective Heat and Mass Transfer 4th Edition. Mcgraw-Hill. 2004

List, M. G., "Numerical Quantification of Interaction Effects in a Closely-coupled Diffuser-fan System." Ph.D. dissertation, University of Cincinnati, Cincinnati, OH. Dec. 2013.

Lucia, David J., Beran, Philip S., Silva, Walter A., “Reduced-Order Modeling: New Approaches for Computational Physics.” Progress in Aerospace Sciences 40. (2004) pp. 51-117

Manwaring, S. R., Rabe, D. C., Lorence, C. B., and Wadia, A. R., "Inlet Distortion Generated Forced Response of a Low-Aspect-Ratio Transonic Fan," ASME Journal of Turbomachinery, 119, 1997, pp. 666-676.

Mathew S. McMullen and Antony Jameson. The computational efficiency of non-linear frequency domain methods. Journal of Computational Physics. (2006): 637-661, 2006.

Mohler, Stanley. "Wind-US Flow Calculations for the M2129 S-duct Using Structured and Unstructured Grids." 42nd AIAA Aerospace Sciences Meeting and Exhibit (2004)

Peterson, Marshall W., "Implementation of Fourier Methods in CFD to Analyze Distortion Transfer and Generation through a Transonic Fan." MS Thesis. Brigham Young University, 2016. Aug, 2016.

Sanders, Darius, Michael List, Chase Nessler, and William Copenhaver. "CFD Performance Predictions of a Serpentine Diffuser Configuration in an Annular Cascade Facility." 51st AIAA Aerospace Sciences Meeting including the New Horizons Forum and Aerospace Exposition (2013)

Smith, Natalie R., William L. Murray, and Nicole L. Key. "Considerations for Measuring Compressor Aerodynamic Excitations Including Rotor Wakes and Tip Leakage Flows." Volume 7B: Structures and Dynamics (2015).

Society of Automotive Engineers, “A Methodology for Assessing Inlet Swirl Distortion,” Aerospace Information Report AIR 5686, October 2010.

Society of Automotive Engineers, "Inlet Total-Pressure-Distortion Considerations for Gas-Turbine Engines," Aerospace Information Report AIR1419, Rev. B, May 2013.

Uranga, Alejandra, Mark Drela, Edward Greitzer, Neil Titchener, Michael Lieu, Nina Siu, Arthur Huang, Gregory M. Gatlin, and Judith Hannon. "Preliminary Experimental Assessment of the Boundary Layer Ingestion Benefit for the D8 Aircraft." 52nd Aerospace Sciences Meeting (2014)

Weiss, J., Subramanian, V., and Hall, K., “Simulation of Unsteady Turbomachinery Flows using an Implicitly Coupled Nonlinear Harmonic Balance Method.” GT2011- 46367. 2011.

APPENDICES

Appendix A. CPU Time Used

Table 8 : Simulation Times			
Model Number	**Mesh Size (Million)**	**Spinning Modes**	**CPU Time (Hours)**
Mesh Sensitivity Study			
1	12	0:3:3/49	6,305
2	15	0:3:3/49	9,469
3	18	0:3:3/49	16,363
Modal Sensitivity Study			
4	15	0:2:2/25	5,954
5	15	0:3:3/49	9,469
6	15	0:4:4/81	10,947
7	15	0:5:5/121	15,506
Parametric Study			
8, a=0.0	15	6:3:0/61	21,034
9, a=0.5	15	6:3:0/61	20,325
10, a=1.0	15	6:3:0/61	20,486
11, a=1.5	15	6:3:0/61	21,089

Appendix B. Using STAR-CCM+ and Setup

Appendix B.1. Steady State Setup of the Fan Simulation

In order to run a simulation with HB, a steady-state solution was required as a start point. Starting the domain pressure ratio at 1.00 and ramping up to its final value of design pressure ratio of 1.92 was completed using the STAR-CCM+ ability to change boundary condition values during computation and add ramp functions. The steady state physics model was set up with the following conditions:

- All y+
- Coupled energy
- Coupled flow
- Gas
- Gradients
- Ideal gas
- Reynolds average Navier stokes
- Spalart-Allmaras turbulence
- Standard Spalart-Allmaras
- Steady

Reference pressure and temperature were set to the values of 14.696 psi and 80º F respectively.

A simulation of turbomachinery required periodic transformation interfaces and mixing plane interfaces. As the geometry used was a sector of the full annulus, the periodic interfaces were used to transport thermodynamic quantities tangentially. Periodic interfaces were set by

selecting the desired boundaries and creating an interface between them. Setting the periodic interface before meshing was a key component in debugging the simulation. Meshing was the only tool in STAR-CCM+ that is able to calculate sector angle.

The mixing plane interface was set up by selecting both boundaries intended for use and implementing an interface between the two. The mixing plane interface was used for the interface between the exit of the rotor region and the inlet of the stator region. This was needed as the reference frame for the rotor region was rotating while the reference frame for the stator was stationary. Once the interface was created, it was necessary to set the interface to implicit connectivity for the steady solution as no nonreflecting boundary conditions were necessary for steady state simulations. The connectivity was subsequently changed to explicit for HB simulations.

Defining boundary conditions was the last step in preprocessing of the steady state solution. All physical blade portions of the computational domain were set to wall conditions. These walls contained prism layers due to the high fluid shear stress on them and include the shroud, blades, and hub. The inlet and outlet were the only unconstrained boundaries and were set to stagnation pressure and outlet pressure, respectively. Stagnation pressure at the inlet was set to 0.0 psi as the reference pressure covers the stagnation inlet to be gage and made it atmospheric pressure. Similarly, the outlet was set to 0.0 psi, making it atmospheric pressure; to begin the run and once converged was increased to mimic the measured design condition of a pressure ratio of 1.92.

Trial and error in the harmonic balance simulations led to the decision of combining the AIP convection region and rotor region into a single region as using three regions rather than two

led to seemingly erratic behavior in the solution and extreme computation time due to the addition of a four spinning mode solution. Difficulties arose when combining the rotor part and convection region due to the meshing technique used and was skirted by first meshing both regions separately and subsequently creating an *in place interface* between the two regions. This allowed the parts to be combined into one region for harmonic balance purposed while ensuring data transfer between the regions.

Grid sequencing was used to implement a better starting solution. This STAR-CCM+ built in function allowed the code to dismember an ultra-fine grid into a coarser one that was able be solved significantly faster. Then the coarse grid solution was interpolated to a finer grid and the starting solution was calculated again. This iterative process continued until the grid is the back to the defined size of 14.9 million elements. Reasonable parameters used for grid sequencing are:

- Maximum grid levels: 10
- Maximum iterations per level: 200
- Convergence tolerance per level: 0.005
- CFL number: 20

The simulation was run to convergence using second order accurate solution schemes. Integrated residual quantities dropped more than four magnitudes and was converged but can go as low as seven magnitudes. Higher magnitudes meant better convergence and the solution approached analytical when the slope of the residual curves were flat.

Appendix B.2 Harmonic Balance Setup of the Fan Simulation

Starting with the previously converged steady state solution several steps were taken before harmonic balance simulations could be completed. First and foremost, the steady state solution previously mentioned must be re-converged after turning on non-reflecting boundary conditions on the inlet, exit, and mixing plane. The number of non-reflecting modes were set to 10. An outlet condition using *radial equilibrium* cannot be used in conjunction with non-reflecting boundary conditions. Because of this fact, the outlet must be set to *pressure outlet*.

With the model converged using non-reflecting boundary conditions, a new physics model was implemented. A new physics continuum was created making use of the harmonic balance physics continuum:

- all y+
- gas
- gradients
- HB
- HB flow and energy
- HB standard Spalart-Allmaras
- ideal gas
- Reynolds averaged Navier stokes
- three dimensional

The same default steady state reference values were used in order to keep simulation parameters consistent. Setting up blade rows and applying blade rows to regions was necessary for HB simulations. The number of blade rows and options were found under the *harmonic*

balance flow and energy tab in continua. Two blade rows were used. The first was the rotor region containing the region upstream of the cone and the second was the stator region.

The number of blades per annulus and pitch were set accordingly to the disk geometry. For instance, the full rotor and stator were composed of 20 and 31 blades, respectively.

STAR-CCM+ defaults the courant number to 50 which was not useable due to the high levels of unsteadiness in the flow. This number was set to 10 upon staring the simulation and was increased to speed up convergence as the residuals began to converge. In addition, per-region partitioning was enabled, using *consider only neighbors* for the frequency compute option.

The number of spinning modes applied to each blade row was important in calculating desired unsteadiness of the region. A higher number of spinning modes provided more insight to the level of unsteadiness found in the region. Work completed by Peterson proved that 1 to 2 modes are sufficient for a performance study while 3 modes were advised for those interested in aeromechanics [Peterson 2016]. These observations matched with the suggestions of CD-Adapco representatives and were supported with a small modal sensitivity study seen in section 4.3.2. However, a (6-3-0) spinning mode triplet was used for the inlet distortion simulations as explained in section 4.3.2.

The model was iterated to convergence. Similar to the steady state solution, a harmonic balance solution is converged when the residuals reach 4 magnitudes and have leveled out. The convergence monitor plots are shown in the following appendix (Appendix C).

Appendix C. HB Residual Plots

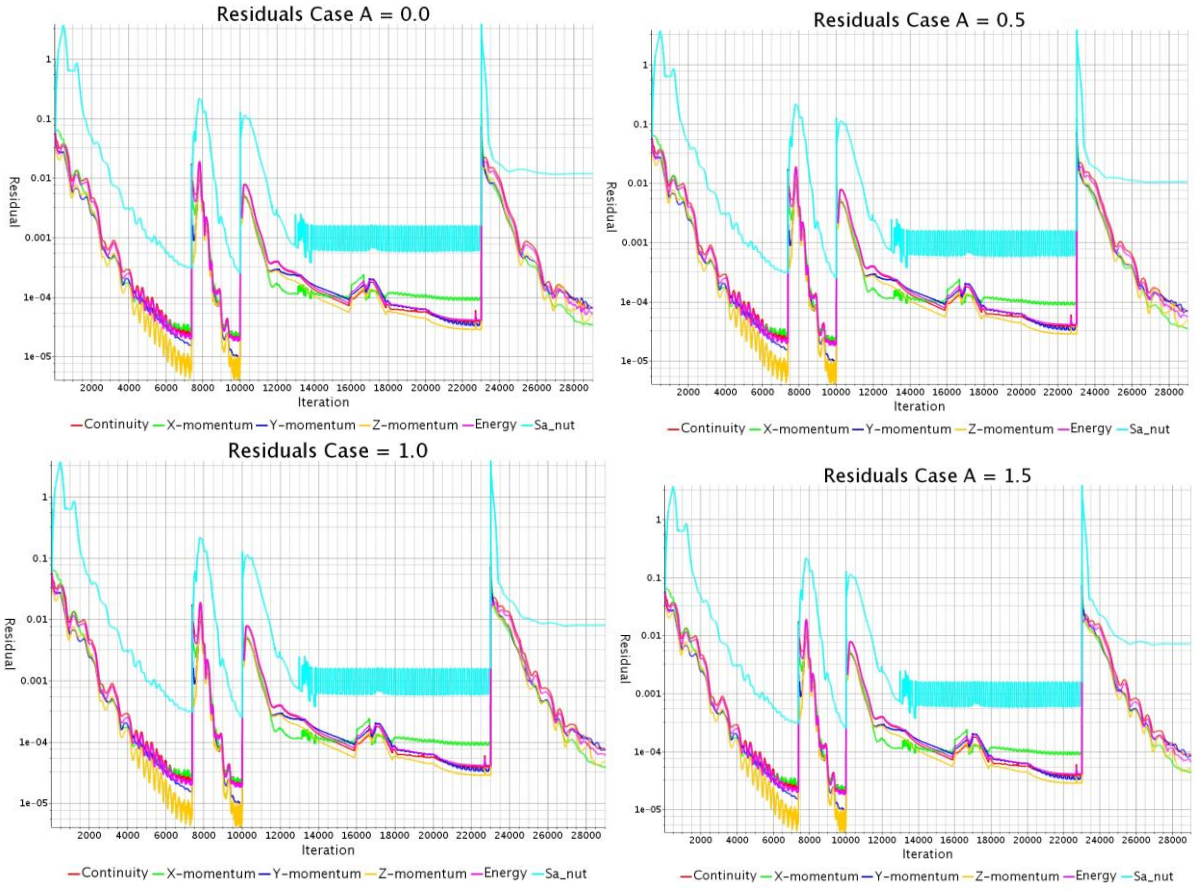

Figure 45 - HB residual plots for parametric case simulations.

Appendix D. SS Simulations Design Value Monitoring

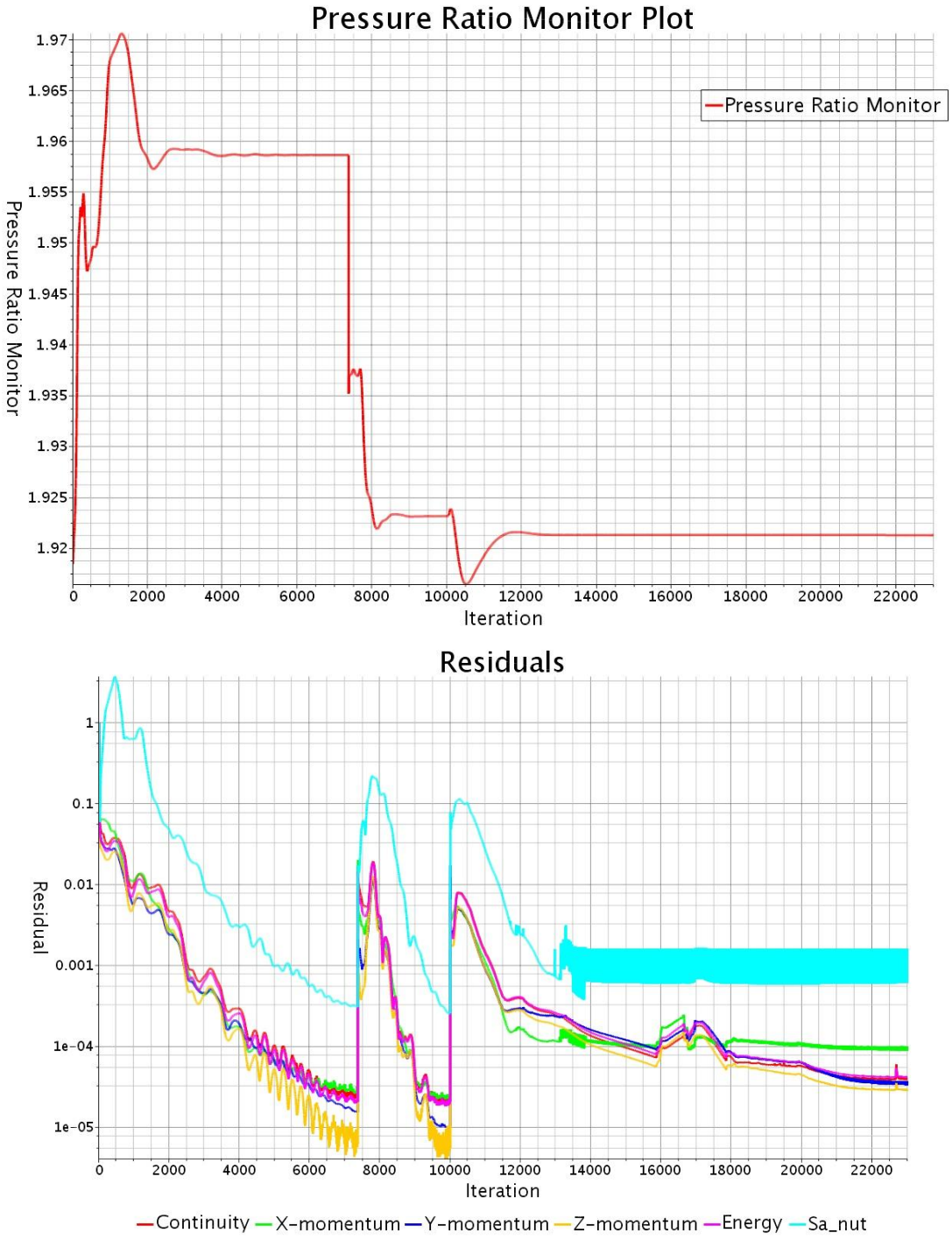

Figure 46 - Steady state pressure ratio monitor plot and steady state residuals plot.